The Thesis Committee for Thomas Alexander Gomez
certifies that this is the approved version of the following thesis:

Examining Line Broadening Approximations using Xenomorph: A Simulation Line Broadening Program

Committee:

Don Winget, Supervisor

Mike Montgomery, Co-Supervisor

Examining Line Broadening Approximations using Xenomorph: A Simulation Line Broadening Program

by

Thomas Alexander Gomez, B.S.

THESIS

Presented to the Faculty of the Graduate School of

The University of Texas at Austin

in Partial Fulfillment

of the Requirements

for the Degree of

MASTER OF ARTS

THE UNIVERSITY OF TEXAS AT AUSTIN

December 2013

Examining Line Broadening Approximations using Xenomorph: A Simulation Line Broadening Program

Thomas Alexander Gomez, M.A.
The University of Texas at Austin, 2013

Supervisor: Don Winget

White dwarfs are particularly interesting due to their broad application to the field of astronomy (cosmochronology, SN Ia progenitors, asteroseismology). Examining distributions of white dwarf masses and temperatures, it is evident that there is some flaw in our ability to make physical atmosphere models. Tremblay and Bergeron (2009) used an *ad hoc* treatment of line broadening and derived significantly different surface gravity and temperatures for white dwarfs, demonstrating the importance of the line broadneing treatment in determining stellar parameters for high surface gravity stars. This thesis presents a new line broadening program, Xenomorph, based on simulation techniques. Xenomorph is used to examine various approximations used in line broadening calculations used in white dwarf atmospheres. Some approximations, like including fine structure and lower state perturbations, have small, if detectable effects. Ion motions during a transition can make features commonly seen in Stark profiles less pronounced and leads to an increase in the

FWHM of the lines. Including a more complete basis set at higher densities will result in extra features, including asymmetries that has been observed in many experiments.

Table of Contents

List of Tables

List of Figures

Chapter 1

Motivation

Ninety-eight percent of all stars will eventually become white dwarfs (WDs), including our sun. Because this is the end point of all stars, WDs are incredibly useful for figuring out the age of the galaxy. WDs are relatively simple objects that cool with time, so the oldest WD would be the coolest. The cores of WDs are very dense and hot, which makes them good astronomical laboratories for studying equations of state. The equations of state studied in cores of WDs are relevant to current research of nuclear fusion. A dark matter candidate, axions, are thought to be be connected with the rate at which WDs cool. Pulsating WDs allow us to "listen" into their interiors and determine their structure. Binary systems with at least one WD are believed to be the projenitors of type Ia supernovae (a thermonuclear explosion when a WD gets massive enough to reach the Chandrasekhar limit, $\sim\ 1.4 M_{\odot}$). Type Ia supernovae can be used as an intergalactic measuring stick and have given us the first clues about dark energy, the mysterious force driving the expansion of the universe. All this interesting science rests on accurately determining the temperature and surface gravity of WDs.

Stellar Properties, such as surface gravity and effective temperature, are

determined by fitting model spectra to an observed spectrum. WDs typically have a log g (surface gravity) that ranges between 5 and 9. An order of magnitude estimate of the density at the photosphere yields 10^{18} atoms/cc (yet, this is still less dense than the air here on Earth). In a hot, dense plasma, there will be many collisions, which will cause the spectral lines to broaden (pressure broadening). The plasma at the photosphere is hot enough for a significant number of the atoms to be ionized. Charged particles near the atom induce an electric field on the radiator, with each atom feeling a different electric field. The atom will then be broadened with the Stark effect.

The basic theory for pressure broadening was developed by Anderson [2]. Baranger [3][4][5] calculated line shapes treating the electron quantum mechanically and found that the results are much the same as the classical path approximation. A Holtzmark distribution was used to describe the electric fields felt by the emitter. Holtzmark distribution is for a classical plasma. Baranger [6][7] and Hooper [21] calculated the electric field distribution function taking into account the screening of electrons in the limit where Debye-Huckel screening is valid (i.e. weakly coupled plasmas).

Hans Griem [20] made a simple semi-analytic calculation for the pressure broadening of hydrogen. The calculation was separated into a fast and slow component, where the slow moving ions are considered static during the transition and the electrons are treated in the impact approximation (standard theory). Kepple & Griem [24], hereafter KG, built on [20] by including more accurate perturbations and using Hooper's distribution. Vidal, Cooper, Smith

[32][40][42][41], hereafter VCS, made benchmark calculations in the 1970s for line broadening that unified the impact approximation with relaxation theory.

Since the 1980s, Stamm [37][36][16] started using computers to simulate plasma conditions to create Stark profiles. The simulations solved Anderson's equations exactly, only approximating the plasma conditions. The plasma simulations allowed them to include ion motions and multi-component plasmas.

These calculated line profiles are used to model white dwarf photospheres. VCS theory (tabulated in [27]) is most popularly used among astronomers (VCS is > 40 years old!!!). Surface gravity is best constrained by the high order (blue transitions) hydrogen lines and temperature is best determined by the lowest lines (green & red transitions).

Kepler et al. [23] analyzed the distribution of derived masses of Sloan Digital Sky Survey WDs, which showed an unphysical increase in mass below 12,000K. Tremblay and Bergeron [39], hereafter TB09, modified VCS to include non-ideal effects proposed by Hummer & Mihalas [22] and Seaton [31]. As a result, the line profiles were narrower and most importantly, when fit to data, produced differences (increases in temperature and density) in the derived plasma properties. The fits by TB09 matched better (than VCS) in the blue wings of the lines and did poorly in the rest of the profile. The result on WD photospheres was a slight increase of mean mass, consistent with the mean mass derived by gravitational redshifts (Falcon et al. [12]).

Falcon et al. [12] measured the gravitational redshift of a large sample

of WDs to determine the mean mass and to see if the 12,000K runaway exists. There are two significant differences between the spectroscopic method and the gravitational redshift method: above 12,000K, the spectroscopically determined mean mass **disagree** by 15%, and at low temperatures, the masses unphysically increase.

The work of TB09 (even though it has the same underlying physics in the profiles) has only demonstrated how important line broadening is to determine stellar parameters. Tremblay and Bergeron have moved on to solve the issue of the runaway effect at low temperatures by introducing 3-D convection. I warrant that the discussion of line broadening is not over and could be significant in determining WD parameters, including increasing the mean mass and removing the low temperature runaway.

In an effort to solve these problems, I will develop a platform to calculate line profiles and examine the approximations used by VCS and TB09. Simulation techniques offer some freedom with testing plasma conditions, but can be computationally expensive, but this will be the method of choice for this thesis. I will discuss the underlying physics of the calculation and examine the effect of various approximations on the line shape.

Chapter 2

Physics of Stark Broadening

2.1 Atomic Physics Primer

Albert Einstein showed in 1905 through the photoelectric effect that light (which has wave-like structure) also exhibits a particle nature. In fact, all particles exhibit this wave-like behavior. The waves (ψ) and their energies will be solutions of the time independent Schrödinger equation:

$$\frac{-\hbar^2}{2m}\nabla^2\psi + V(\overrightarrow{r})\psi = E\psi, \tag{2.1}$$

where V is some potential felt by the particle, m is the mass of the particle, E is the energy of the state, and $\hbar$ is the reduced Planck constant. The Schrödinger equation is an eigenvalue equation and can be written,

$$H\psi = E\psi, \tag{2.2}$$

where H is the Hamiltonian operator that contains $\frac{-\hbar^2}{2m}\nabla^2 + V(\overrightarrow{r})$ and E is the eigenvalue. If the potential is zero, then the solution is an oscillatory function based on the energy of the particle. In a box (two potential barriers that trap a particle), the energy of the particle takes specific values (quantization of energy), where the lowest energy state has the lowest integral number of wavelengths inside the box. This is analogous to the fundamental frequency

of a musical instrument. Like a musical instrument, there will be overtones that will include different integral number of waves that fit in the box. Each wave overtone will have different, distinct energy.

The basic structure of an atom (Bohr model) is a heavy, positively charged nucleus at the center and light electrons orbiting the nucleus. The hydrogen atom is a special case where the potential is the electric coulomb potential (e^2/r) due to the proton at the center. Due to the wave-like behavior of electrons in an atom, the electron does not orbit like planets around the sun, but rather has an integer number of spherical waves around a spherically symmetric potential. These spherical waves can be described by a separable wave-function with a radial wave solution multiplied by an angular solution given by spherical harmonics:

$$\psi = R_{nl}(r)Y_m^l(\theta, \phi), \tag{2.3}$$

where R is the radial function, the Y_m^l is the spherical harmonic function. Quantum numbers are used to describe a specific wave-function of an electron: principle, orbital, and magnetic (denoted n, l, m, respectively). The orbital quantum number (for hydrogen) ranges from $0 \leq l \leq n-1$, and the magnetic quantum number ranges from $-l \leq m \leq l$. For historical reasons, the different l states are described with letters to avoid confusion with other quantum numbers (see table 2.1).

Parity is a measure of symmetry of the wave-function ($P\psi(r) = \pm\psi(r)$), where P is the parity operator. If the wave-function is symmetric, then it has

Table 2.1: Angular Momentum Quantum Number Designations

l	0	1	2	3	4	5	6	7	8	9	10
	s	p	d	f	g	h	i	k	l	m	n

even parity ($P\psi(r) = +\psi(r)$)and if the wave-function is asymmetric, then it has odd parity ($P\psi(r) = -\psi(r)$). States with even l (0,2,4) have even parity and states with odd l have odd parity.

When referring to a state, one usually writes only the principle quantum number and the orbital quantum number, n and l, respectively. For example, an electron in the $n = 2$, $l = 0$ state is denoted '$2s$'. Parity is not often used to describe a hydrogenic state. The energy eigenvalues for a one electron system are

$$E = -\frac{Z^2}{n^2} Ry, \tag{2.4}$$

where Z is the nuclear charge and Ry is the Rydberg unit of energy (13.6eV = 1Ry).

The electron has an intrinsic spin, s, with eigenvalue, m_s that takes values of $\pm\hbar/2$. The two angular momentum quantum numbers couple together, called LS coupling, to make $l + s = j$, the total angular momentum. The total orbital angular momentum (in general) is $L = \sum_i l_i$. Total spin, S, can also be written in the same way, $S = \sum_i s_i$. Total angular momentum, like S and L, can be written as the sum over individual angular momenta, $J = \sum_i j_i$. The term of an atomic state is denoted ${}^{2S+1}L_J$ where the S is the total spin, L is the total orbital angular momentum, and J is the total angular momentum ($J = L + S$). Including the spin of the electron causes

a small break in degeneracy and leads to fine structure in the atomic energy levels. The energy eigenvalues then have the following form:

$$E = -\frac{Z^2}{n^2} - \frac{Z^2}{n^2}\left[\frac{\alpha^2}{n^2}\left(\frac{n}{j+\frac{1}{2}} - \frac{3}{4}\right)\right], \tag{2.5}$$

where α is the fine structure constant. There are other effects that cause structure to arise that is smaller even than fine structure: Lamb shift (QED effects) and hyperfine structure (spin of proton). Fine structure will not be important for Stark shapes of Hydrogen Balmer transitions above an electron density $\sim 10^{14} e^-$/cc and will be ignored in the line shape calculations presented here. This is advantageous because the fewer states to consider, the faster the calculation will be performed.

2.2 Dipole Moments, Selection Rules, and Radiative transitions

The classical electric dipole moment, $\vec{D}$, is classically defined as $e\vec{r}$, where e is the electric charge and $\vec{r}$ is the position of the object from some reference point. The quantum mechanical electric dipole moment evaluates $\vec{r}$ as an expectation value of $\vec{r}$. Since the wavefunctions are a probability amplitude, the expectation value can be evaluated as an integral over wavefunctions:

$$\vec{D} = e\int_{-\infty}^{\infty} \psi^*(\vec{r})\vec{r}\psi(\vec{r})d^3\vec{r}. \tag{2.6}$$

Selection rules will determine which combination of states have non-zero dipole moments There is *no dipole moment* of a state with itself and only states with opposite parity will have a non-zero dipole moment.

The integration over the angular parts can be evaluated using properties of the spherical harmonic functions and can be described using a 3j symbol (See §C.2.1). The dipole moment can be separated (See AppendixA on Bra-Ket notation)

$$\langle \psi_{nlm} | D_q | \psi_{n'l'm'} \rangle = \begin{pmatrix} l & 1 & l' \\ -m & q & m' \end{pmatrix} \langle \psi_{nl} \| D \| \psi_{n'l'} \rangle, \tag{2.7}$$

where q defines the vector component, the 3j symbol accounts for the angular integration, and the reduced dipole moment, $\langle \psi_{nl} \| D \| \psi_{n'l'} \rangle$, is the radial integral, the physical quantity of interest, defined as

$$\langle \psi_{nl} \| D \| \psi_{n'l'} \rangle = (-1)^l \sqrt{(2l+1)(2l'+1)} \begin{pmatrix} l & 1 & l' \\ 0 & 0 & 0 \end{pmatrix} e \int_0^\infty R^*_{nl}(r) r R_{n'l'}(r) dr, \tag{2.8}$$

[1]

where the 3j symbol imposes a selection rule that requires l to change by 1 unit of angular momentum, i.e. a change in parity. An example of the selection rule for parity change is the $n = 2$ to $n = 1$ transition of hydrogen. $\langle 2s \| D \| 1s \rangle = 0.0$ because there is no change in l, the selection rules from Eq (2.8) result in a zero dipole moment (forbidden transition). However, $\langle 2p \| D \| 1s \rangle$ is not zero because the selection rule is satisfied and there is a nonzero dipole moment (dipole allowed transition).

The reduced dipole moment is a scalar, unlike the total dipole moment which is a vector quantity. The reduced dipole moment can be transformed

[1] A simple transformation using a 6j symbol (§C.2.2) would include fine structure in the reduced dipole moment: $\langle \psi_{nlj} \| D \| \psi_{n'l'j'} \rangle = \delta_{s,s'} (-1)^{l+s+j'+1} \sqrt{(2j+1)(2j'+1)} \begin{Bmatrix} j & 1 & j' \\ l' & s & l \end{Bmatrix} \langle \psi_{nl} \| D \| \psi_{n'l'} \rangle$.

using a tensor operator (3j symbol) to rotate it into components of a vector:

$$\begin{aligned} D_- &= \begin{pmatrix} J & 1 & J' \\ -M & -1 & M' \end{pmatrix} \langle \alpha J \| D \| \alpha' J' \rangle &= \tfrac{1}{\sqrt{2}}(D_x - \imath D_y) \\ D_0 &= \begin{pmatrix} J & 1 & J' \\ -M & 0 & M' \end{pmatrix} \langle \alpha J \| D \| \alpha' J' \rangle &= D_z \\ D_+ &= \begin{pmatrix} J & 1 & J' \\ -M & 1 & M' \end{pmatrix} \langle \alpha J \| D \| \alpha' J' \rangle &= \tfrac{-1}{\sqrt{2}}(D_x + \imath D_y). \end{aligned} \tag{2.9}$$

The selection rules of the 3j symbols require that $|J - J'| \leq 1$, $J \neq 0$, and that the sum of the bottom terms be zero. Therefore $M - M' = q$ where q is the middle bottom number. The different values of q correspond to different polarization transitions. If $q = 0$, then this is a π transition, which is linearly polarized in the z-direction. If $|q| = 1$, then this is a σ transition, circularly polarized in the x-y plane.

Electrons can transition between different states of the atom. This is made possible by the absorption or emission of a photon. The transition probability of an electron to spontaneously go from an upper state to a lower state (assuming a two level atom) is defined by an Einstein A coefficient [11]:

$$A_{ul} = \frac{4}{3\hbar c} \frac{e^2}{4\pi\epsilon_0 c^2} \omega^3 \sum_{q,M} |D_{q,m}|^2 \tag{2.10}$$

where we write the square of the dipole moment as

$$|\vec{D}_{q,M}|^2 = \langle nljm | \vec{D} \cdot \vec{D} | n'l'j'm' \rangle = \begin{pmatrix} j & 1 & j' \\ -m & q & m' \end{pmatrix}^2 \mathbf{S}, \tag{2.11}$$

where $\mathbf{S}$ is the line strength or the square of the reduced dipole moment. Electrons can also go from an upper state to a lower state stimulated by

radiation (B) instead of spontaneous decay. Einstein was able to relate the stimulated emission to the spontaneous absorption by

$$B_{i,j} = A_{i,j}\frac{c^3}{8\pi h\nu^3}. \tag{2.12}$$

Stimulated emission was not expected but was necessary to reproduce the Planck spectrum ($B_\nu(T) = \frac{2h\nu^3}{c^2}(exp(h\nu/kT) - 1)^{-1}$). The absorption of light is related to the stimulated emission by the ratio of the degeneracy, g, of the upper and lower states: $g_i B_{ij} = g_j B_{ji}$ [11].

The absorption cross section can be described by the classical electric dipole harmonic oscillator, with a correction factor

$$\sigma = \frac{\pi e^2}{m_e c} f \tag{2.13}$$

where f is the correction factor called the oscillator strength. The oscillator strength can be written

$$f = \frac{2m_e\omega}{3\hbar} g \sum \begin{pmatrix} J & 1 & J' \\ -M & q & M' \end{pmatrix}^2 \mathbf{S}. \tag{2.14}$$

2.3 Stark Effect

Everything I have described above would be accurate if there were just one atom in the universe. Our understanding of atomic physics changes when we bring in a second atom or charged particle in close proximity. In this case, there may be electric fields, magnetic fields, or overlapping wavefunctions from other nearby atoms. This is the reason why the subject of line broadening has

been continuously studied over the years. In dense, ionized plasmas, the atom feels a strong electric field. I will discuss some of the observed changes when an atom has an electric field induced upon it.

Stark (1913) first observed the effects of an electric field on an atom. The energies of the levels split, similar to the Zeeman effect. Solving for the energy eigenvalues can be done exactly using parabolic coordinates (not discussed here), or using perturbation theory. Perturbation theory takes a known state, applies an external potential and looks for corrections to the energies and wavefunctions. One can use a variety of approximations to determine corrections to the energy eigenvalues. the analytic first order correction remove the degeneracy of n and the energy eigenvalues are linear (neglecting fine structure) as a function of electric field. Second order corrections are quadratic with electric field and higher order corrections can be used to get more accurate results.

Using the matrix formalism, put forth by Heisenberg, the perturbed energy eigenvalues can be found numerically with modern computational techniques. The Hamiltonian matrix elements for the Stark effect (in [9] notation) are shown in Equation (2.15) where $\vec{D}$ is the dipole operator and $\vec{F}$ (to avoid confusion with energy eigenvalues) is the electric field, in Rydberg units.

$$\langle \alpha JM | H_{Stark} | \alpha' J' M' \rangle = -2\vec{F} \cdot \langle \alpha JM | \vec{D} | \alpha' J' M' \rangle \tag{2.15}$$

The electric field is often chosen to be aligned with the z-axis. Note that

there are no diagonal elements because the electric dipole moment requires a parity change between the two states. See Figure 6.1 for the Stark effect on the $n = 2$ level of hydrogen including fine structure.

At small electric field (when fine structure is included) the energy levels will be quadratic as a function of electric field. Once the off diagonal elements of the Stark effect become larger than the energy separation due to fine structure, the energy eigenvalues become linear with electric field. When including matrix elements that connect different n, the high electric field effects can then be reproduced, such as the quadratic behavior of the ground state.

The new wavefunctions can be described by a linear combination of unperturbed wavefunctions that form a basis set,

$$\psi = \sum_n c_n |n\rangle, \tag{2.16}$$

normalized so that $\sum_n |c|^2 = 1$, where c_n is the probability amplitude. Therefore, the new $2s$ state will become a linear combination of the other $n = 2$ states. As a result of the mixing, parity and total angular momentum are no longer good quantum numbers, but m remains a good quantum number.

The new reduced dipole moments can be evaluated as

$$\langle \alpha \| \check{\mathbf{D}} \| \beta \rangle = \sum_n \sum_m c_n^* c_m \langle n \| D \| m \rangle \tag{2.17}$$

Where n and m are the pure states that form the basis set of the Hamiltonian. α and β are the mixed states. Due to Stark mixing, a $2s \rightarrow 1s$

transition **will be allowed.** The evolution of the c_n^2 of one of the $2p$ states is shown in Figure 6.2.

2.4 Broadening

In partially ionized plasmas, each atom feels a different electric field, therefore lines are not split (like what is observed in static global magnetic field), but broadened. The line instead is broadened. In high density plasmas, the spectral lines are broadened so much that thermal broadening has little effect on the profile. $\Delta n =$ even transitions have no unshifted central component, resulting in a central dip. For example, Hβ has a central dip and Hγ has a central peak.

Since the work of Anderson [2] it has been well established that line shapes can be calculated by the Fourier transform of the dipole auto-correlation function:

$$L(\omega) = \Re \int_{-\infty}^{\infty} e^{-\imath\omega t} \langle C(t) \rangle_{av} dt. \tag{2.18}$$

The autocorrelation function, $C(t)$, is defined as the trace of the dipole evolution with the initial dipole matrix: $Tr\{\vec{D}(t) \cdot \vec{D}(0)\}$. The dipole moment evolution can be evaluated by using the time evolution operator: $\vec{D}(t) = U^{\dagger}(t)\vec{D}(0)U(t)$. The time evolution operator is the solution to the Schrödinger equation of the form:

$$\imath\hbar \frac{\partial}{\partial t} |\psi(t)\rangle = H|\psi(t)\rangle. \tag{2.19}$$

The evolution of the eigenstates can be described by a time evolution operator, $U(t)$, that can evolve the states: $|\psi(t)\rangle = U(t)|\psi(0)\rangle$. The Schrödinger equation can be rewritten to solve for the time evolution operator instead of ψ. The solution will take the form:

$$U(t) = e^{-\imath \int_0^t H(t)dt/\hbar} = \sum_n e^{-\imath \int_0^t E_n(t)dt/\hbar} |n\rangle\langle n|, \tag{2.20}$$

where the set of E_i are the eigenvalues and $|i\rangle$ are the corresponding eigenstate solutions of the Schrödinger equation (though I will emphasize that time ordering of this integral is important). Any function of an operator, $f(\hat{O})$, can be written as function operating on the eigenvalue over the set of eigenfunctions that satisfies the Schrödinger equation, $f(o)|\psi\rangle$.

During a transition, an electron will oscillate between two bound states. The Stark effect changes the energies and eigenvalues slightly as a function of time and will cause there to be changes in the "vibrational frequency". When there is an ensemble of atoms, all of which have changing frequencies, the oscillations will be out of phase and destructively interfere which causes the auto-correlation, C, function to decay.

This is analogous to the attack of a bell, or other percussion instrument. The attack has many frequencies that overlap and create an unique sound, the different frequencies will cancel each other out and the vibrations damp out.

The Fourier transform of a flat line is a delta function and vice versa. Therefore, a transition that takes longer to damp out will have a sharper peak. A transition that damps out quickly will have a wider profile. From here on,

when I mention the auto-correlation function, I will refer to the amplitude variation with time, not the trivial oscillations (transition frequency). In calculations, removing the high frequency oscillations aids in reducing numerical errors. Figures 6.4 and 6.6 show examples of auto-correlation functions for Lyα and Lyβ.

The Fourier transform of a decaying function (see section on natural & pressure broadening) will have a central component and Lorentzian wings. The amplitude of Lyβ becomes negative before it decays to zero and will have a double peak structure when Fourier transformed.

2.4.1 Natural & Pressure Broadening

It is well established that states have a finite lifetime. Due to the Heisenberg uncertainty principle, the finite lifetime of the state will have an uncertainty or spread in the energy of the state. As a result, when the electron in some upper state spontaneously decays to a lower state, the lines have some finite width in energy. I will write the Hamiltonian

$$H = H_{atom} - \imath\Gamma, \tag{2.21}$$

where $\hbar = 1$, H_{atom} is the Hamiltonian of the field free atom and Γ is the relaxation operator that describes the lifetime of the state. The relaxation operator can be a sum of both the natural lifetime of the state and timescale for collisions with electrons (or some other perturber). Equation (2.18) can be

written as

$$L(\Delta\omega) = \int_{-\infty}^{\infty} dt\ e^{-\imath(\omega-\omega_0)t} d^2 e^{-\Gamma t} \tag{2.22}$$

where ($\Delta\omega = \omega - \omega_0$). This Fourier transform of a decaying exponential should be familiar:

$$L(\Delta\omega) = d^2 \frac{\Gamma/2\pi}{\Delta\omega^2 + (\Gamma/2\pi)^2} \tag{2.23}$$

Equation (2.23) is the familiar Lorentzian function.

2.4.2 Voigt Profile

The Voigt profile is a convolution of a Doppler and Lorentzian profiles. This technique combines the thermal broadening of a plasma with the natural shape of the line. Voigt profiles will then take on the shape of a Doppler (Gaussian) core and Lorentzian wings. Using the Fourier transform definition of convolution, then the Voigt profile can be written in a natural way.

$$L(\Delta\omega) = \int_{-\infty}^{\infty} dt e^{-\imath(\omega-\omega_0)t} d^2 e^{-\Gamma t} e^{-t^2/\sigma^2} \tag{2.24}$$

will be the Fourier transform of the Voigt function where σ is the width of the Doppler profile.

2.4.3 Standard Stark Broadening Theory

Stark broadening theory is based on Anderson's Fourier transform method of calculating the line profile for hydrogen. The first assumption made in the 1960s and developed by KG, VCS was that electron impacts are very fast

compared to those of H^+. The Hamiltonian takes the form:

$$H = H_{atom} + V_{ion} + V_{elec} \tag{2.25}$$

where in the impact limit,

$$V_{ion} = -d \cdot \vec{F} \quad \text{and} \quad V_{elec} = -\imath\Phi(t). \tag{2.26}$$

$\Phi(t)$ is the impact operator that averages over the Stark effect due to the fast motion of the electrons. The impact limit is valid when the time between collisions is long compared to the duration of a collision. Baranger [5][3] has demonstrated that treating the electrons as quantum particles gives the same results as treating them as classical particles. Therefore, very few Stark broadening calculations for hydrogen have treated the electrons as quantum particles. Φ can be calculated in a number of forms.

I will neglect any discussion of the plasma charge oscillation frequency for this thesis, but it needs to be taken into account for more precise line shapes, since it has been observed in several experiments as small satellite lines. For our conditions of interest, plasma frequency satellites will show up at intervals of order $\sim 0.01eV$. The amplitude of the plasma frequency oscillations are a few percent of the average field generated by free particles and will be difficult to detect in most experiments.

Anderson's equation then takes the form:

$$L(\Delta\omega) = \int_{-\infty}^{\infty} d^2 \langle e^{-\imath(\omega-\omega_0(\vec{F}))t} e^{-\Phi t} \rangle_{av} dt. \tag{2.27}$$

The averaging can be re-written as an integral over a distribution of electric fields. This can easily be done when the ions are assumed to be static. In the case of hydrogen, this may not be a valid approximation (see §5.2), but for higher Z elements, this will be a good approximation. To include the distribution over electric microfields, the equation for a Stark broadened line takes the form:

$$L(\omega) = \int_0^\infty W(\vec{F}) I(\vec{F}, \omega) d\vec{F}, \tag{2.28}$$

where W is the electric field distribution and I contains the information about the collisions with electrons. I have used $\vec{F}$ as the symbol for the electric field to avoid confusion with energy eigenvalues.

If the impact approximation is assumed, then the form of I in frequency space takes the form using matrix element formalism, [20][28]:

$$I(\omega, \vec{F}) = -\frac{1}{\pi} \Im \sum_{a,a'} \rho_a \mathbf{d}_{af} \mathbf{d}_{fa'} \left[\omega - \Delta\omega(\vec{F}) - \Phi(\omega) \right]^{-1} \tag{2.29}$$

is a general Lorentzian where ω is the frequency, $\Delta\omega$ is the shift in frequency due to the Stark effect, and $\Phi(\omega)$ is the impact operator. The impact operator can be a constant or frequency/time dependent. This impact operator averages over electron configurations and impacts and can be modified to take into account penetrating collisions [1]

The VCS and TB09 theory takes the form of (2.28). VCS [32] unifies the relaxation and one electron impact theories, which is claimed to be more general and accurately describes the electron contribution to the line profile from the core to the wings.

These calculations have agreed well with experiment, in particular Wiese et al. [44], with strong agreement in the wings of the lines. However, VCS failed to account for asymmetries in the high density profile and overpredicted central structure. The FWHM of VCS profiles have been used as plasma diagnostics ever since their work.

TB09 attempted to take into account the effect of electric field ionization by integrating only over electric fields where the electron is still bound to the atom. The line shape equation is modified as initially proposed by [31].

$$L(\omega) = \frac{\int_0^{F_{crit}} P(\vec{F}) J(\omega, \vec{F}) d\vec{F}}{\int_0^{F_{crit}} P(\vec{F}) d\vec{F}}, \tag{2.30}$$

where $F_{crit} = \frac{2n+1}{6n^4(n+1)^2} \frac{e}{a_0^2}$. To account for ionization due to electronic collisions, TB09 created a high frequency cutoff in the profile, where they define ω_c as the ionization threshold frequency according to the linear Stark effect. The profile is then modified a second time to account for this:

$$L'(\Delta\omega) = \frac{L(\Delta\omega) e^{-|\Delta\omega|/\omega_c}}{\int_0^{\infty} L(\Delta\omega) e^{-|\Delta\omega|/\omega_c} d\omega}, \tag{2.31}$$

where $\Delta\omega$ is defined as the detuning, $\omega - \omega_0$, where ω_0 is the transition frequency. Using this approximation, TB09 have calculated profiles beyond the limits of the approximations used. For example, the impact approximation is not valid at high densities. The impact approximation for $H\delta$ is no longer valid above 10^{17} e/cc. When the lines get fat, the decay time is short, which means that even electrons will be in the quasi-static limit.

2.4.4 Simulation Methods

By the 1960s computers became incredibly useful in solving problems, including line broadening. In the 1970s, a method was proposed to create Stark profiles by solving Anderson's equations exactly and simulating the electric field sequence. Stamm et al. [36], [37] showed that it was possible to simulate a plasma as an N-body simulation, simulating an evolving electric field at the position of the emitter, solving the Schrödinger equation to calculate the auto-correlation function. The calculated auto-correlation function is then averaged over many electric field time sequences. [16] was the first to implement this method to the Balmer series of H, simulating only 80 particles.

The method is a classical N-body plasma simulation, usually with great care taken to calculate the re-injection of particles that leave the simulation. Using Monte-Carlo methods, it is possible to simulate two temperature plasmas or even plasmas that do not obey Maxwellian statistics.

In certain regimes treating the electrons as classical is not a bad approximation, as long as the typical length between particles is much greater than their de Broglie wavelength, $l_{typ} \gg r_{deBroglie}$, where $l_{typ} = (n_e \frac{4}{3}\pi)^{-1/3}$ and the thermal de Broglie wavelength is $\sqrt{h/2\pi mkT}$ for an ideal gas. Quantum effects become important when the typical distance between particles becomes of order the thermal de Broglie wavelength (see Figure 6.7). This assumption of an ideal gas is good as long as the plasma remains weakly coupled. A plasma is weakly coupled when Hooper's 'a' value (l_{typ}/r_{Debye}) is less than 1.

There are actually very few collisions with the nucleus itself, but the electrons will reside inside the "sphere of influence" of an ideal plasma which is described by the Debye radius (equation (2.32)).

$$\lambda_D = \sqrt{\frac{k_B T}{4\pi n_e e^2}} \tag{2.32}$$

Where k_B, T, n_e, e are the Boltzmann constant, temperature, electron density, and electric charge, respectively. When neglecting particle-particle interaction, Stambulchik et al. [34] [33] uses different effective Debye lengths for different species in the plasma. The Debye length used is the general form

$$\lambda_D = \sqrt{\frac{k_B T}{n_e e^2/T_e + \sum_i n_j q_j^2/T_j}}, \tag{2.33}$$

where j denotes the different species in the plasma and q_j is the charge of that element in the plasma. Each species is then screened by other like species and lighter particles Therefore, only electrons can contribute to screening of electrons, while ions are subject to screening by both ions and electrons.

Therefore, [34] has the above formula for electrons and reduces the Debye length for the ions, since ion motion will screen other ions. The electric field is determined (in 3-D space) as a function of time, using a charge shielded electric field for the perturbers,

$$\vec{F} = \frac{e}{r^2}\left(1 + \frac{r}{\lambda_D}\right) e^{-r/\lambda_D}. \tag{2.34}$$

The Hamiltonian is solved at every time step. The time step must be small enough to resolve the electric field and oscillations of the autocorrelation

function. If the sampling is not fine enough, then the motions of the particles may be over-predicted (close to the atom) or may result in errors in the auto-correlation function. However, oversampling will increase computing time.

The perturbations by the electrons and ions are the same, where V_{ion} and V_{elec} are both the Stark effect ($-d \cdot \vec{F}$). The only interaction the atom has with the plasma is through the electric field. Electrons will be quick relative to the ions and will have quick, sharp spikes in electric field, while the ions will create the background electric field. In this picture, the spikes in electric field will cause a phase shift in the auto-correlation function. When averaged, this will reproduce the behavior of a decaying exponential. The Fourier transform will recreate the Lorentzian shape commonly seen in Stark profiles.

Chapter 3

Calculation

3.1 Plasma E-field Simulation

I have built an N-body simulation to create a time sequence of electric fields at the atom placed at the center of the simulation sphere. My simulation sphere is chosen to be 7 Debye lengths in order to simulate enough particles, but not so large that it slows computation. I assume that the plasma is weakly coupled and close to ideal. This assumption can simplify the calculation when I choose the plasma particles to move in straight line trajectories (i.e. ignore particle-particle interaction) according to an impact parameter distribution. Stambulchik et al. (2007) [33] have shown that only in strongly coupled plasmas is accounting for particle-particle interaction important; at $T_e = 1eV$ and $n_e = 10^{18}$ the errors in the FWHM are $\sim 10\%$. In the case of hydrogen, the emitter is neutral, so I need not take into account radiator-perturber interactions. For charged emitters I will change the trajectory to be hyperbolic or parabolic trajectories as an alternative to simulating all particle-particle interactions in the plasma.

Using random number techniques [30], I randomly create impact parameters, b, for the particles, sampled from the distribution $P(b) = b\sqrt{R_{sim}^2 - b^2}$

[16]. Initial particle positions generated are greater than that particle's corresponding impact parameter. The particles must move within the simulation for several crossing times to redistribute the particle positions, making it uniform. I compare an electric field distribution function from this method with Hooper's low frequency electric field distribution (See Figure 6.10). Velocities are sampled from a Maxwellian distribution, where direction is determined by the impact parameter.

When perturbers leave the simulation sphere, they are put back at a random position on the edge of the simulation sphere. The magnitude of velocity is kept the same in order to avoid cooling. If the particles were to be re-injected at a random angle, the random number generator would favor larger angles, causing the electrons to drift away from the atom. To prevent this, the velocity direction is chosen to preserve the same impact parameter. To achieve this, the particle is first placed at the top of the sphere, $x = 0$, $y = 0$, $z = r_{sim}$. The velocity polar angle defined as $\theta_{vel} = \arctan(b/r_{sim})$, and the azimuthal angle is chosen at random. A random θ and ϕ are chosen for the particle's new position, and rotation matrices are then used to change the coordinates from the top of the simulation to the chosen random position on the simulation edge.

The atom is placed at the center of the simulation sphere and will feel the electric field of all the particles. The electric field felt by the radiator is the sum of all the perturbers in the plasma. Each particle will have the Debye-Hukel screened electric field (See eqn (2.34)). The Debye length used

to screen the electrons will have contributions only from other electrons. The Debye length for the ions will have contributions from both the electrons and moving ions. This is a slight overestimate of the Debye length of the ions, but is more accurate than having it singly screened [33].

3.2 Time Evolution Operator

I will get the necessary information (unperturbed energy eigenvalues and reduced dipole moments) from the analytic equations in [8]. For elements other than hydrogen, I can use Cowan's [9] atomic spectroscopy code to get these same quantities. I have neglected fine structure because these effects are unimportant at the temperatures and densities of interest and only increase calculation time by adding twice the number of states considered. [29] examined the fine structure of Hα and found significant changes in the line shape up to $n_e = 10^{14}$. Figure 6.12 shows that there is no difference between including and neglecting fine structure for our temperature and density of interest. The energy eigenvalues will be diagonal elements of the Hamiltonian. Therefore, when there is no perturbation, then the returned eigenvalues are the diagonal elements.

The electric field produced by the simulation will be transformed into the coordinates outlined in §C.1. The off diagonal matrix elements for the

Hamiltonian for the Stark effect are evaluated

$$\langle \alpha JM|H_{elec}|\alpha' J'M'\rangle = -2(-1)^{J-M}\langle \alpha J\|D\|\alpha' J'\rangle \times \left[\mathfrak{C}^{J1J'}_{-M0M'}F_z - \mathfrak{C}^{J1J'}_{-M1M'}\frac{F_x+\imath F_y}{\sqrt{2}} + \mathfrak{C}^{J1J'}_{-M-1M}\frac{F_x-\imath F_y}{\sqrt{2}}\right], \quad (3.1)$$

where the "$\mathfrak{C}$"s are the 3j symbols $\left[\mathfrak{C}^{j_1j_2j_3}_{m_1m_2m_3} = \begin{pmatrix} j_1 & j_2 & j_3 \\ m_1 & m_2 & m_3 \end{pmatrix}\right]$

The reduced dipole matrix, D, for Lyα will take the form (with actual values of the unperturbed reduced dipole matrix elements):

$$\begin{array}{c} \\ 1s \\ 2s \\ 2p_1 \\ 2p_0 \\ 2p_{-1} \end{array} \begin{array}{c} \begin{array}{ccccc} 1s & 2s & 2p_1 & 2p_0 & 2p_{-1} \end{array} \\ \begin{pmatrix} 0 & 0 & 1.29 & 1.29 & 1.29 \\ 0 & 0 & 0 & 0 & 0 \\ 0 & 0 & 0 & 0 & 0 \\ 0 & 0 & 0 & 0 & 0 \\ 0 & 0 & 0 & 0 & 0 \end{pmatrix} \end{array}, \quad (3.2)$$

where the states are labeled as nl_m, n is the principle quantum number, l is the orbital angular momentum, and m denotes the azimuthal or magnetic quantum number. The Hermitian conjugate of the reduced dipole transition matrix is $D^\dagger$

$$\begin{array}{c} \\ 1s \\ 2s \\ 2p_1 \\ 2p_0 \\ 2p_{-1} \end{array} \begin{array}{c} \begin{array}{ccccc} 1s & 2s & 2p_1 & 2p_0 & 2p_{-1} \end{array} \\ \begin{pmatrix} 0 & 0 & 0 & 0 & 0 \\ 0 & 0 & 0 & 0 & 0 \\ -1.29 & 0 & 0 & 0 & 0 \\ -1.29 & 0 & 0 & 0 & 0 \\ -1.29 & 0 & 0 & 0 & 0 \end{pmatrix} \end{array}. \quad (3.3)$$

There will be two methods that I will discuss for solving the time evolution operator U. U takes on different definitions depending on the quantum representation used (§B). The Schrödinger representation evolves the amplitudes of the eigenstates, while the Heisenberg representation evolves the operators. The latter is a good representation to use when doing matrix mechanics. U is used to evolve state vectors ($|\psi(t)\rangle = U(t)|\psi(0)\rangle$) and to evolve operators ($A(t) = U^{\dagger}(t)AU(t)$). Both representations have been used in this program and are found to yield the same results. Since the Hamiltonian takes the form of a known atomic solution and a time dependent perturbation, I can take advantage of the interaction picture.

3.2.1 Eigenvalue Solver

I will solve for the eigenvalues and eigenvectors to advance the time evolution operator, finding the time evolution with Schrödinger's equation. I am using a method described in [10], [18], and [17] to solve for the time evolution operator. Advancing the time evolution operator can be written as a series of products:

$$U(t_i) = U(t_{i-1})U(t_{i-2})....U(t_0). \tag{3.4}$$

Where each advancement in time can be written

$$U(t_i) = exp\left[\frac{\imath}{\hbar}\int_{t_{i-1}}^{t_i}\hat{H}(t)dt\right]U(t_{i-1}) \tag{3.5}$$

and can be numerically evaluated as

$$U(t_i) = \left[\sum_n e^{-\imath E_n(t_{i-1})\Delta t/\hbar}|n(t_{i-1})\rangle\langle n(t_{i-1})|\right]U(t_{i-1}). \tag{3.6}$$

$E_n(t)$ will be the eigenvalue at time, t, and $|n(t)\rangle$ will be the corresponding eigenvector solution. The argument inside the sum is explicitly written

$$e^{-\imath E_n(t_{i-1})\Delta t/\hbar}|n(t_{i-1})\rangle\langle n(t_{i-1}) = \\ e^{-\imath E_n(t_{i-1})\Delta t/\hbar}\begin{pmatrix} c_1^*(t_{i-1}) & c_2^*(t_{i-1}) & \dots \end{pmatrix}_n \begin{pmatrix} c_1(t_{i-1}) \\ c_2(t_{i-1}) \\ \vdots \end{pmatrix}_n , \tag{3.7}$$

where each n is an eigenvalue solution with its corresponding eigenvector whose amplitudes are represented by the c's. Using this form provides numerical stability, keeping the time evolution operator unitary. I will remove the high frequency component of the transitions to reduce numerical errors in the Fourier transform,

$$\mathcal{U}(t) = e^{iH_0t/\hbar}U(t). \tag{3.8}$$

From here on out, I will define $\mathcal{U}$ as the low frequency changes in the time evolution operator. I will use the Heisenberg representation to evolve the dipole moments: $D(t) = \mathcal{U}^\dagger(t)D\mathcal{U}(t)$. When Fourier transforming this form of the dipole moment, bigger steps can be taken. Time steps also do not need to be small to sample transition frequencies. Because the high frequency oscillations can be taken out, the Fourier transform has less numerical noise.

3.2.2 Numerical Integrator

I will use the interaction picture to check that I get the same profiles. The Schrödinger equation in the interaction picture removes the high frequency oscillations of the unperturbed part of the Hamiltonian, H_0

$$i\hbar\frac{d}{dt}\mathcal{U}_I(t) = e^{iH_0t/\hbar}V(t)e^{-iH_0t/\hbar}\mathcal{U}_I(t), \tag{3.9}$$

to solve the time evolution operator with the subscript denoting the interaction representation. I can use different integrators, for example, the simple Euler integration takes the form

$$\mathcal{U}_I(t+\Delta t) = \mathcal{U}_I(t) + \Delta t \left[\frac{-i}{\hbar} e^{iH_0 t/\hbar} V(t) e^{-iH_0 t/\hbar}\right]. \tag{3.10}$$

But Euler integration has stability problems, which is going to be problematic when V(t) varies with time. The Runge-Kutta (RK) method [30],[34] modifies the Euler integration:

$$\begin{aligned}
k_1 &= \frac{-i}{\hbar} e^{iH_0 t/\hbar} V(t) e^{-iH_0 t/\hbar} \mathcal{U}_I(t) \\
k_2 &= \frac{-i}{\hbar} e^{iH_0 t/\hbar} V(t) e^{-iH_0 t/\hbar} \left[\mathcal{U}_I(t) + \frac{\Delta t}{2} k_1\right] \\
k_3 &= \frac{-i}{\hbar} e^{iH_0 t/\hbar} V(t) e^{-iH_0 t/\hbar} \left[\mathcal{U}_I(t) + \frac{\Delta t}{2} k_2\right] \\
k_4 &= \frac{-i}{\hbar} e^{iH_0 t/\hbar} V(t) e^{-iH_0 t/\hbar} \left[\mathcal{U}_I(t) + \Delta t k_3\right] \\
\mathcal{U}_I(t+\Delta t) &= \mathcal{U}_I(t) + \frac{\Delta t}{6}\left[k_1 + 2k_2 + 2k_3 + k_3\right].
\end{aligned} \tag{3.11}$$

The different k_i predict the integrated function, but has issues due to some large electric fields due to strong collisions. In order to compensate, the time steps must be very small. *This has a disadvantage of needing smaller time steps to insure that the time evolution operator maintains unitarity.* If the time evolution operator exceeds the initial value, then the run is repeated with a different set of initial conditions. Even with a small time step, $\mathcal{U}$ does not always stay unitary and often runs away. This method is not desirable due

to the lack of stability. Due to the extra time-steps required, the RK method is slower than using the eigenvalue solver. At low and moderate densities the RK solution and eigenvalue solutions are indistinguishable. If the no-quenching assumption is made (§5.3), the high density profiles are near identical. But when taking into account the effect of other states (and including effects of field ionization), then the profiles have the same shape, but may not necessarily have the same width. Because the RK method does not guarantee unitarity, there may be artificial broadening that is numerical nature [10]. Figure 6.11 illustrates this with a high density Hβ profile.

3.3 Autocorrelation Function

When I calculate the auto-correlation function, I want to remove the trivial high-frequency and look for low frequency modulations in the amplitude since including the high frequency oscillations makes no difference in the basic line shape (except at high electric fields) and introduces unphysical features on the blue side of the profile. Looking for the amplitude reduces numerical noise in the Fourier transform and allows me to reduce the number of time steps in the calculation.

The time evolution operator will only be operating on the reduced dipole moments, the physical quantity of interest (see Appendix §C.1). The evolved dipole matrix, $\check{\vec{\mathbf{D}}}$ is written as:

$$\check{\vec{\mathbf{D}}} = \mathcal{U}^{\dagger}(t)\vec{D}\mathcal{U}(t)e^{\imath\Delta\omega t}. \tag{3.12}$$

The frequency $\Delta\omega$ is centered around the transition of interest (when fine structure is considered). Once I have this matrix, I can then use an identity for the scalar product of two tensor operators based on the orthogonal properties of the 3j symbols.

$$\langle \alpha JM|\overrightarrow{D}\cdot\overrightarrow{\check{\mathbf{D}}}|\alpha' J'M'\rangle = \sum_{\alpha'' J''}\langle \alpha J\|D\|\alpha'' J''\rangle\langle' \alpha J''\|\check{\mathbf{D}}\|\alpha' J'\rangle\times$$

$$\sum_{m''q}(-1)^{-q+J-M}\begin{pmatrix} J'' & 1 & J \\ -M'' & q & M\end{pmatrix}(-1)^{-j''+m''}\begin{pmatrix} J'' & 1 & J' \\ -M'' & q & M'\end{pmatrix} \tag{3.13}$$

can be simplified using 3j symbol identities:

$$\langle \alpha JM|\overrightarrow{D}\cdot\overrightarrow{\check{\mathbf{D}}}|\alpha' J'M'\rangle = \delta_{JM,J'M'}\frac{1}{2J+1}\sum_{\alpha'' J''}(-1)^{J-J''}\langle \alpha J\|D\|\alpha'' J''\rangle\langle \alpha'' J''\|\check{\mathbf{D}}\|\alpha' J'\rangle. \tag{3.14}$$

This simplification is much faster because it does not need to call the 3j function repeatedly. The dipole moment is then evolved to evaluate the autocorrelation function

$$C(t) = \left\langle Tr\{U(t)D^{\dagger}U^{\dagger}(t)\cdot D\}\right\rangle_{av}. \tag{3.15}$$

3.4 Multiple Lines

I can modify equation (3.15) to include multiple lines. This is worth the modification because at high densities the lines begin to overlap and treating each line as a series of pseudo-two-level-atom may not be appropriate. The

equation for the autocorrelation function would need to be modified to include a density matrix:

$$C(t) = \left\langle Tr\{U(t)D^{\dagger}U^{\dagger}(t) \cdot D\rho\} \right\rangle_{av}. \tag{3.16}$$

The density matrix, ρ is defined as an occupation probability and can be described by Boltzmann factors,

$$\rho = e^{H_{atom}/kT}/Tr\{e^{H_{atom}/kT}\}. \tag{3.17}$$

If the level populations are not in LTE, the density matrix may be difficult to calculate. However, in our density and temperature range, describing populations with Boltzmann statistics is sufficient, even if the states may not be in absolute LTE.

The Fourier Transform of multiple lines can be numerically inaccurate, so I will present an alternative for the calculation where the evolved dipole matrix is averaged first. The Fourier transform $D(t)$ is performed before the multiplication of the unperturbed dipole moment. Since I am using a mean (or a sum) to average the different runs, then I can move the average inside the trace,

$$\langle Tr\{D(t) \cdot D\}\rangle_{av} = Tr\{\langle D(t)\rangle_{av} \cdot D\rho\}. \tag{3.18}$$

Matrix calculus identities allows me to move the Fourier transform inside the trace of the autocorrelation function,

$$\int_0^{\infty} e^{-i\omega t} Tr\{\langle D(t)\rangle_{av} \cdot D\}dt = Tr\left\{\int_0^{\infty} e^{-i\omega t}\langle D(t)\rangle_{av}dt \cdot D\rho\right\}, \tag{3.19}$$

where I define the dipole moment as a function of frequency,

$$\langle D(\omega)\rangle_{av} = \int_0^\infty e^{-i\omega t}\langle D(t)\rangle_{av} dt. \tag{3.20}$$

The line shape function then takes the form

$$L(\omega) = Tr\{\langle D(\omega)\rangle_{av} \cdot D\rho\} \tag{3.21}$$

for emission. Absorption line shapes take the same form, but ρ is changed to be $\rho_i - \rho_u$. This form is a numerically simple way to calculate the entire hydrogen spectrum and can even be used for the single line case.

Chapter 4

Comparisons & Testing

In this short section I perform checks against past work to insure that my calculations agree for the same approximations. Since Hβ is the standard (where many theories agree) and has been used extensively as a diagnostic, it is important to compare my Hβ profile with VCS and Gigosos et al. [13], both of whom have extensive tabulated line widths and profiles. Both [13] and VCS did use the *no-quenching approximation* (See §5.3). Table 6.1 compares my values of the Hβ FWHM against [13]. The FWHM agree well. Making the same assumptions as VCS (static ions, linear stark effect, screened electrons), my simulated profiles are identical (within numerical noise) for $\log_{10} n_e$ between 15 and 18 (see Figures 6.13 and 6.15). My calculations agree over at least 3 orders of magnitude! The excellent agreement with past work gives me an excellent foundation to test assumptions commonly made in line broadening theory of hydrogen.

Figure 6.16 tests the effects of increasing Δt. For the highest quality profiles, Δt must be taken to be small because larger time-steps diminish the wings. This may be a small effect in the overall profile, but recall that the wings of the profile are important for calculating gravities in WDs. Figure 6.17 also

shows the effect of the number of configurations on the profile, testing at what point the profile converges. Obviously, increasing the number of configurations will increase the quality of the profile.

Chapter 5

Line Shapes & Approximations

5.1 Limitations & Considerations

I have assumed that the only interaction the plasma has with the atom is through the electric dipole moment. This means I have not accounted for the quadrupole moment Stark effect in my calculations or even the effects of neutrals. The plasma conditions of interest to us will not require a quadrupole moment with the electric field. At higher densities (i.e. for strongly coupled plasmas), it will be necessary to include the quadrupole effects. I am treating the electrons as classical, but have justified this approximation in Figure 6.7. This is a fine approximation for the temperatures and densities that we are interested in for WD photospheres. Baranger [5][3] has shown that quantum mechanical treatment of electrons has little effect on the line shape. But for more strongly coupled plasmas where the thermal de Broglie wavelength is the the same order of magnitude as the mean separation of the particles, then the electrons must be computed quantum mechanically.

The inclusion of close interactions of the perturbers with the atom have not been considered. For example, as ions get close, a quasi H_2^+ state can form, creating weak satellite lines. I have also neglected to include the

effects of penetrating electron collisions on the atom [1], which is difficult to incorporate in a simulation method. Accounting for penetrating collisions requires solving the Schrödinger equation using a non-uniform electric field.

There is another effect I have not included explicitly in my calculations that has to do with electric field ionization [8]. At sufficiently high electric fields (where the electric field is no longer a perturbation) the line shapes will dissolve into a continuum. If the electric field energy is of the same order as the the ionization energy of the state, there is a high probability that the electron will become ionized, reducing the strength of the transition and contributing to the continuum opacity. The experiment by [44] shows that the higher order transitions dissolve into the continuum. TB09 tried to take this into account by truncating the integral over electric microfields (Eq (2.30)) and resulted in a narrowing of the profiles. There is no good theory to describe the line shapes of lines that are at the threshold of ionization.

In my calculation of the Schrödinger equation, it's ideal to use an infinite basis set. Obviously this is not realistic, so I need to include a cut-off that will accurately calculate line shapes without compromising computing time. Solving the Schrödinger equation is the most computationally expensive part of the calculation. Therefore the more states I include in the calculation, the longer it takes. Lyα requires only 10 states, so this is a very quick calculation. If I were to do the full set (up to $n = 12$), I would need nearly 1000 states. Doing the standard theory using the full set is easy because the Schrödinger equation needs to be solved only a couple of hundred times. In a simulation,

I need to solve more than a thousand time steps per iteration and I am doing hundreds to ten thousand iterations, meaning I am solving the Schrödinger equation from 500,000 to 10s of millions of time during a calculation. Instead of including all the possible states, I will only include the two states adjacent to the line (see §5.3). Including the extra states will not form a complete basis, but will account for 1^{st} order changes in the line shape. More computing power is required in order to do these calculations with a more complete basis.

5.2 Dynamic Ions

It has been suggested in the literature ([44], [35], [14]) that static ions is not a valid approximation when testing accuracy of line shapes.

[35] suggested that ion dynamics could account for some of the discrepancies in the cores of lines and developed a simulation technique for plasmas to be able to include this effect. [14] compared the profiles of the Balmer series using the μ-ion model. In the "μ-ion" model, the ions are given the velocity according to a Maxwellian distribution defined by the reduced mass of the radiator-perturber system. Dynamic ions will "blur" the profiles and fill in the dip as well as broaden the line more. Figure 6.18 uses Hβ as an example to demonstrate the effects of ion dynamics. Transitions where there is a central component will also be affected. Static ions create "shoulders" in Hγ. Due to the "blurring" of the line, the shoulders will disappear and the profile will look more Lorentzian. Figure 6.19 shows significant changes in the profile of Hα. At reasonably high densities, the FWHM increases 66% compared to the

static ion case. Dynamic ions (for hydrogen) corresponds to a $\mu = 0.5$, while dynamic radiator and static ions is $\mu = 1.0$, and static ions and static radiator is $\mu = \infty$.

The effect of dynamic ions will be more important for narrower lines. Narrower lines need more time for $C(t)$ to decay. If there is more time, then the ions will move before the transition is done. At $n_e = 10^{15}$, The FWHM of Hδ increased by 7.25%. With Hα with the most dramatic change and Hδ with small but non-negligible changes in the FWHM, ion collisions and fluctuations can affect the shape of the line, changing the interpreted conditions. Inclusion of ion dynamics might account for some of the runaway effect observed in Kepler et al. (2007).

5.3 Interacting States

When solving the Stark effect, it is important to account for the interaction of states between different principle quantum numbers. This means that the calculation includes a more complete basis set. At low densities, where perturbations due to the electric field are small, there is little contribution to the line. However, at high densities, where the perturbations are of the same order as the energy separation of the different n transitions, then this will change the shape of the line.

When I ignore the matrix elements that connect different n, the energy eigenvalues are linear for arbitrarily large electric fields, which is unphysical. Interactions between states (even at low electric fields) introduce extra struc-

ture, some of which can be approximated by 2^{nd} and 3^{rd} order Stark effects.

Hα is a good example to demonstrate the effects of nearby states [34]. Ignoring interactions between $n = 2$ and $n = 3$, will create a symmetric profile centered on the transition energy (i.e. no shift). However, if the interaction between $n = 2$ and $n = 3$ is included, then Hα will shift to the blue and the FWHM will be relatively unchanged. Including $n = 4$ will cause the line center to shift red-ward of the unperturbed transition energy and asymmetries will begin to surface, though will be more apparent on the higher order lines. In the Balmer series, the blue side of the core is enhanced due to this effect, while the red wing is enhanced (See Figures 6.11 and 6.21).

At high densities, Hβ shows significant asymmetries (see Figure 6.11) in the core. The wings of Hβ do not have the same intensity, with the blue side being diminished and the red side enhanced, opposite of the core. However, when the perturbations are strong (energy eigenvalues overlap), then the lines become diminished, Figure 6.20 demonstrates this for Hϵ. Therefore in the experiment by Wiese et al., we see that the peak is shifted toward the blue because the red side of profile ceases to exist. The shapes of Hδ and Hϵ are reproduced well by including this effect, and also shows that the line is narrower because the energy eigenvalues cannot expand beyond this limit.

This concept of including other states is not new, [10], [34], [18], [25] used this in their calculation of line profiles, but not for the transitions at our temperatures and densities of interest for WD photospheres. [44] pointed out some of the failures of VCS to accurately predict the asymmetries in both

the line core and the wings. By including a more complete basis set, the asymmetries are reproduced (Figures 6.24,6.25,6.26).

5.3.1 Comparison with Experiment

I will compare my profiles against VCS and TB09 using the Wiese et al experiment as the benchmark. This is a good experiment to compare to due to its high signal-to-noise ratio and high spectral resolution. The compared profiles have the fewest assumptions (See §5) To compare, I have included the ω^4 factor in the emission

$$j_\nu(\omega) = \frac{e^2}{3\pi c^3}\omega^4 \mathbf{S}. \tag{5.1}$$

I then add an arbitrary 1^{st} order polynomial background to account for the b-f continuum and I scale so that the profile height matches the height of the experiment values. The high density spectrum was determined to be $\sim 9\times10^{16}$ Wiese et al. The fit by Xenomorph is $\sim 1\times10^{17} e/cc$, so the profiles from Figure 6.21 are appropriate.

The fits between Hβ, Hγ, and Hδ are pretty consistent with the mean $(1.086 \pm 0.0097) \times 10^{17}$ and the standard deviation is 0.017×10^{17}, which is 1.5% of the mean.

Figure 6.24 compares the Hβ profile calculated with Xenomorph. I have agreement in both the core and the wings of the line. I am confident that dynamic ions and including quenching collisions and field ionization is the most accurate model for the line shapes. The asymmetry and depth of the dip of the Hβ core are reproduced exactly. VCS and TB09 over predict the

structure of the central dip.

The estimate from this calculation is slightly higher than the density determinations from the continuum fit ($\sim 10\%$) due to including ion motion in the Debye length. The derived fit is within the uncertainties of the fit and the estimate.

Figure 6.25 compares the Hγ profiles calculated by Xenomorph and Wiese et al. The ion dynamics have reduced the "shoulder" structure and reproduced the profile nearly identically. All three theories are nearly identical for this line.

Figure 6.26 compares the Hδ profiles calculated by Xenomorph and Wiese et al. This transition will be crucial to picking out the proper line broadening model. Accounting for ion dynamics washes out the central structure of Hδ and is currently the only line broadening code to accurately predict no central dip. This is also the only calculation to predict the knee in the core.

Chapter 6

Conclusions

In this thesis I have examined line broadening of H in order to better determine atmospheric parameters of white dwarfs. The main focus was to examine the various approximations used. The various approximations include ignoring ion motion, and ignoring quenching collisions. Some approximations are valid in certain regimes, for example, fine structure effects are not noticeable at electron densities above 10^{14} e/cc.

Accounting for ion dynamics can lead to a blurring of the features of the Stark broadened line. In hydrogen, this does have an effect on the line shapes and can cause some discrepancies in the FWHM. The effect will be more pronounced for narrower lines (lower electron density). At 12,000K, VCS underestimates the width of the line, ion dynamics may be able to correct this effect. Because I am accounting for ion motion, I have reduced the Debye length for the ions. This will cause a slight reduction in the FWHM of the lines ($\sim$ 10%). The reduction in the FWHM will lead us to infer a higher density, which would increase determined the log g of white dwarfs

Including the nearby n states will create a more complete basis set. This reproduces the observed asymmetries in the Balmer series. The effect

is more pronounced at higher densities where the perturbation due to the electric field is of the same order of magnitude as the energy splitting between the different levels.

I have also been able to include magnetic fields more self-consistently in my calculations which has not been done in H before. This may allow us to get better parameters on B fields in WD. Zeeman splitting may go undetected in low resolution spectra of WDs. In order to detect Zeeman splitting, the splitting must be greater than the average electric field from the plasma. The theory developed here will be in place to interpret the coming experiments at Sandia National Laboratories and aid in accurately constraining surface B fields in observed WDs.

Using as few assumptions as possible when fit to data (Wiese et al. 1972), Xenomorph outperforms TB09 and VCS in reproducing the line shapes. Xenomorph profiles as a density diagnostic has agreement between Hβ, Hγ, and H$\delta \sim 1\%$.

I will be the first to use simulation techniques on the higher order lines for conditions in WD photospheres. Never before have the higher order lines been properly treated for the effects of the nearby states.

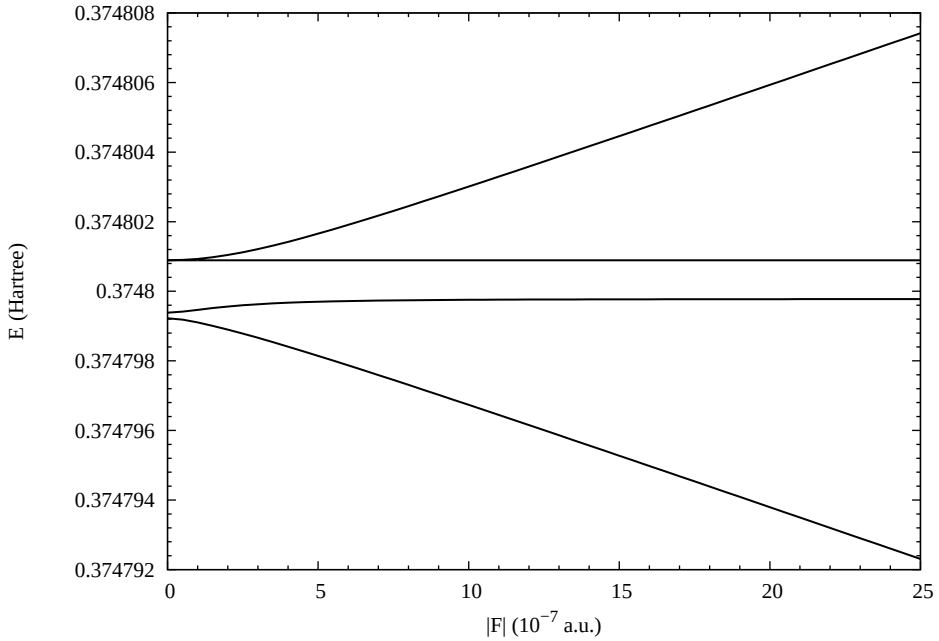

Figure 6.1: The Stark effect on the energy eigenvalues for the $n = 2$ states of H. The upper-most state is the $2p$ $j = 3/2$ $m = 1/2$ state. The unperturbed state is the $2p$ $j = 3/2$ $m = 3/2$ state. The state that parallels the unperturbed state is the $2s$ $j = 1/2$ $m = 1/2$ state and the lowest state is the $2p$ $j = 1/2$ $m = 1/2$ state. Notice that only states that have the same m are perturbed.

Table 6.1: Comparing Hβ

$T_e(K)$	n_e	FWHM (Gigosos)	FWHM (This work)	% difference
10,000	1×10^{14}	0.397	0.401	1.0
10,000	1×10^{15}	2.16	2.12	1.8
10,000	1×10^{16}	10.2	9.5	7.3
20,000	1×10^{18}	233	233	< 1.0

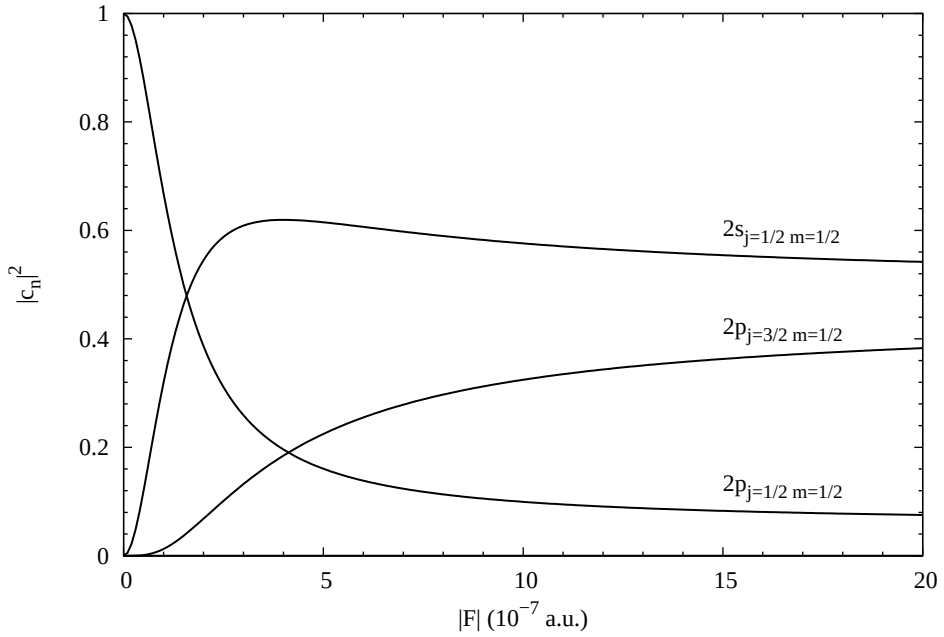

Figure 6.2: The Stark effect on the eigenfunctions for the $2p$ state where $j = 1/2$ $m = 1/2$. Notice that there is a non-zero component of the $2s$ state and the other $2p$ states. $2p$ $j = 3/2$ $m = 3/2$ has no component because states of different magnetic number do not mix.

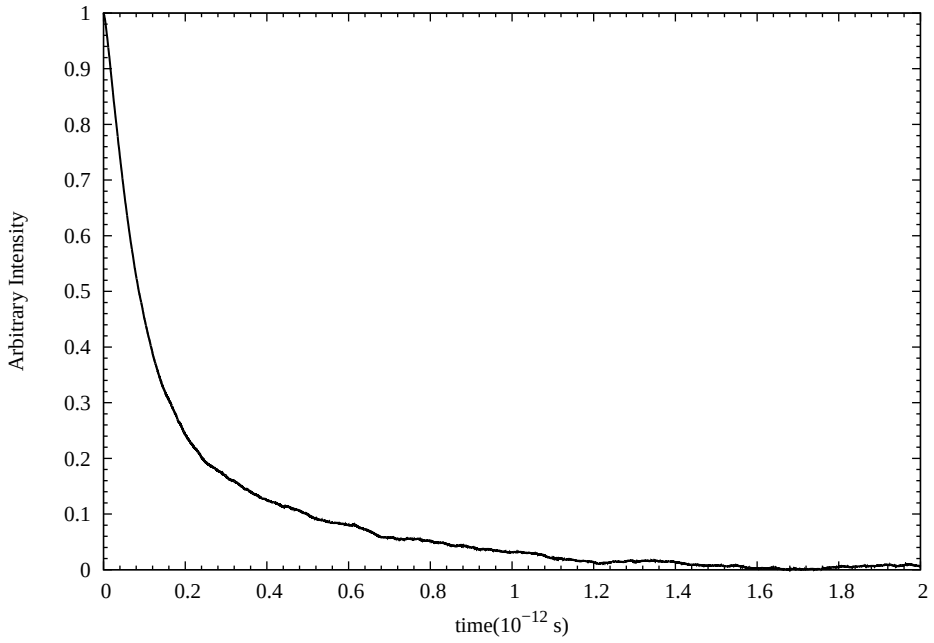

Figure 6.3: The auto-correlation function of Lyα.

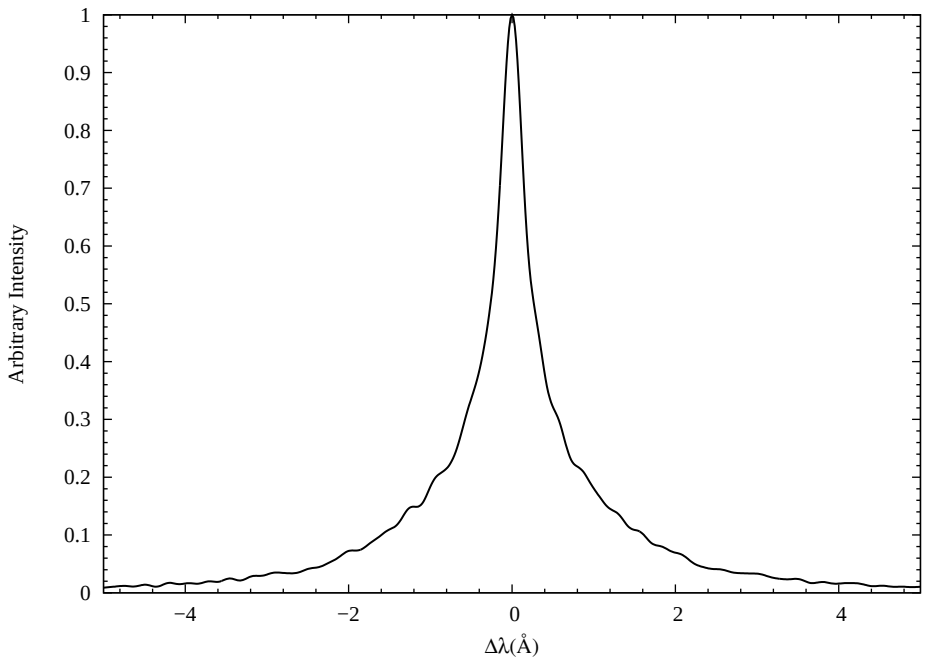

Figure 6.4: The spectra of Lyα. The exponential decay of the function Fourier transforms to be Lorentzian in shape.

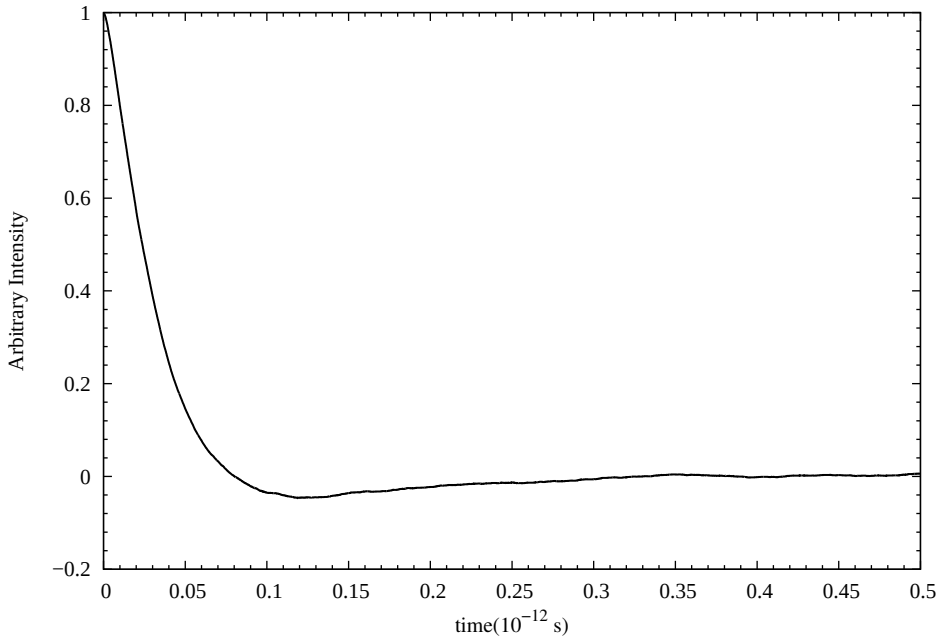

Figure 6.5: Left: The auto-correlation function of Lyβ. Right: The spectra of Lyβ. The auto-correlation function has a dip in this case, which will lead to a dip in the spectrum.

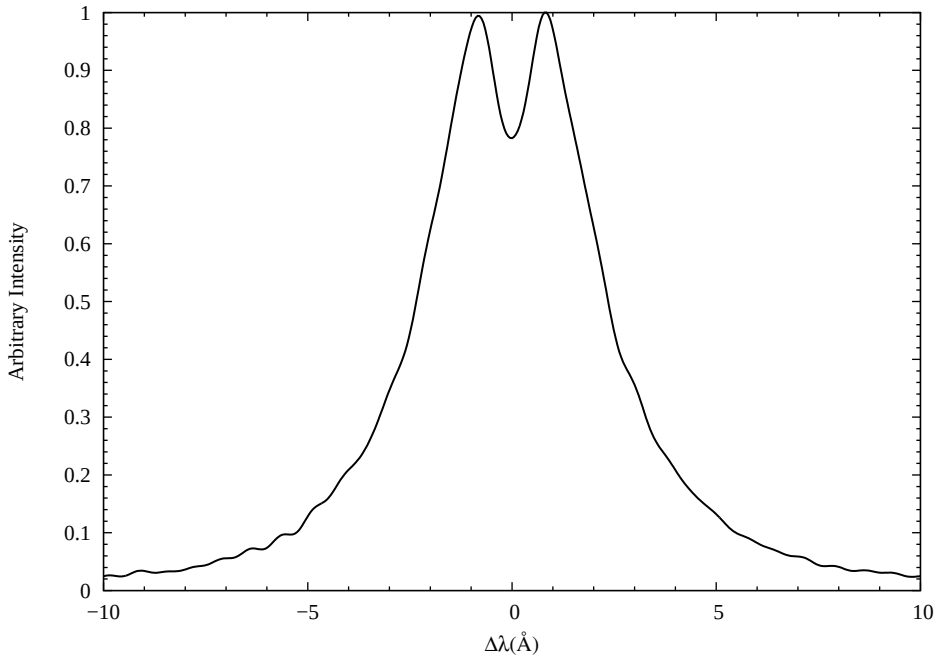

Figure 6.6: Left: The auto-correlation function of Lyβ. Right: The spectra of Lyβ. The auto-correlation function has a dip in this case, which will lead to a dip in the spectrum.

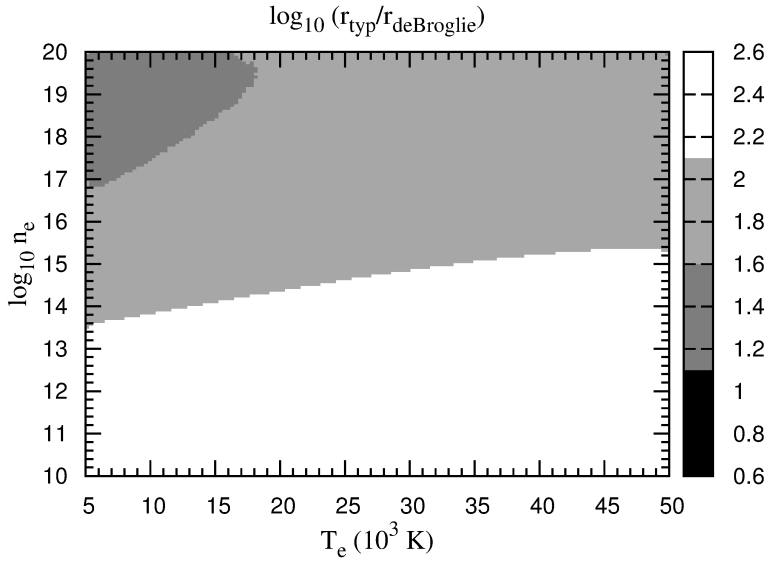

Figure 6.7: The contour of the ratio of the typical distance to the de Broglie wavelength. The log is plotted, any black part of the region would be cause for concern to assume electrons as classical particles. Assuming classical electrons for our temperature and density regime is appropriate.

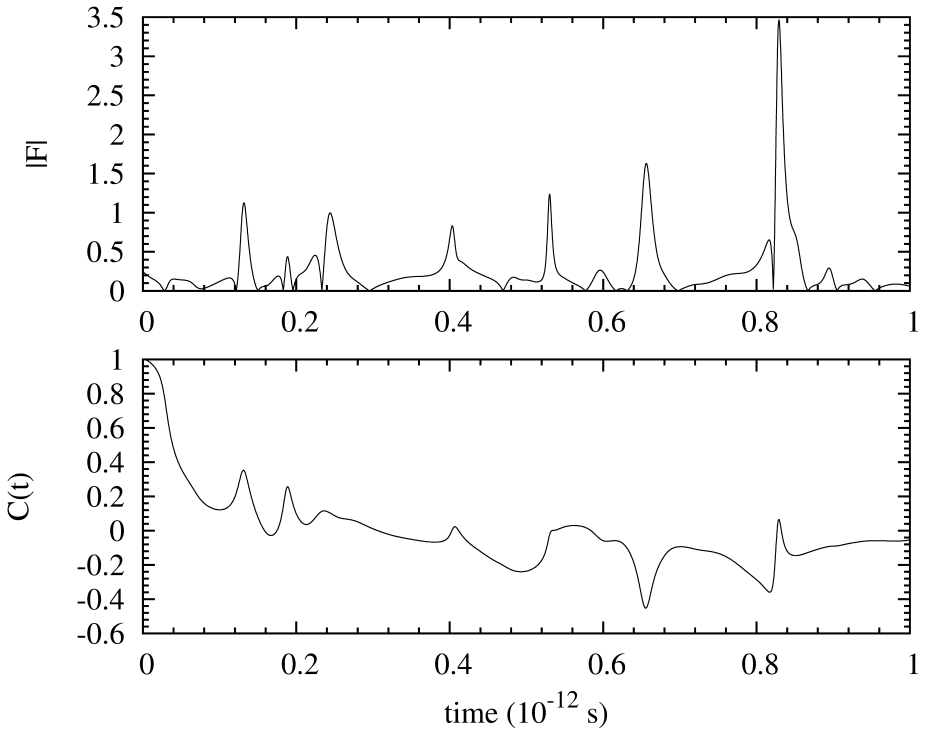

Figure 6.8: Top: A simulated electric field as a function of time. Bottom: the auto-correlation function for the same F field sequence shown above.

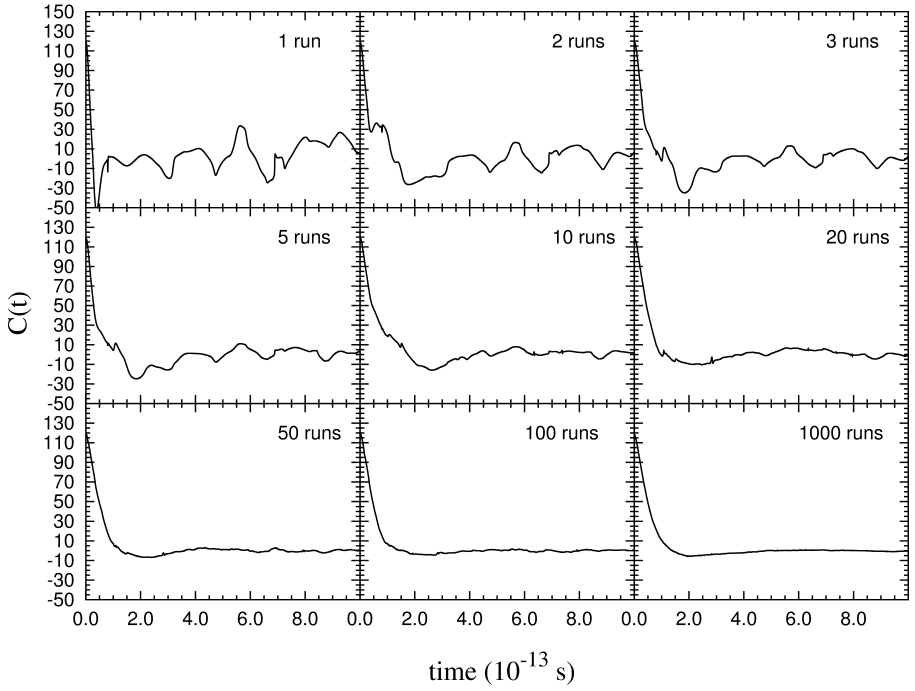

Figure 6.9: Showing the evolution of the auto-correlation function with an increasing number of runs, showing the final shape for a transition in the plasma with an increasing number of runs.

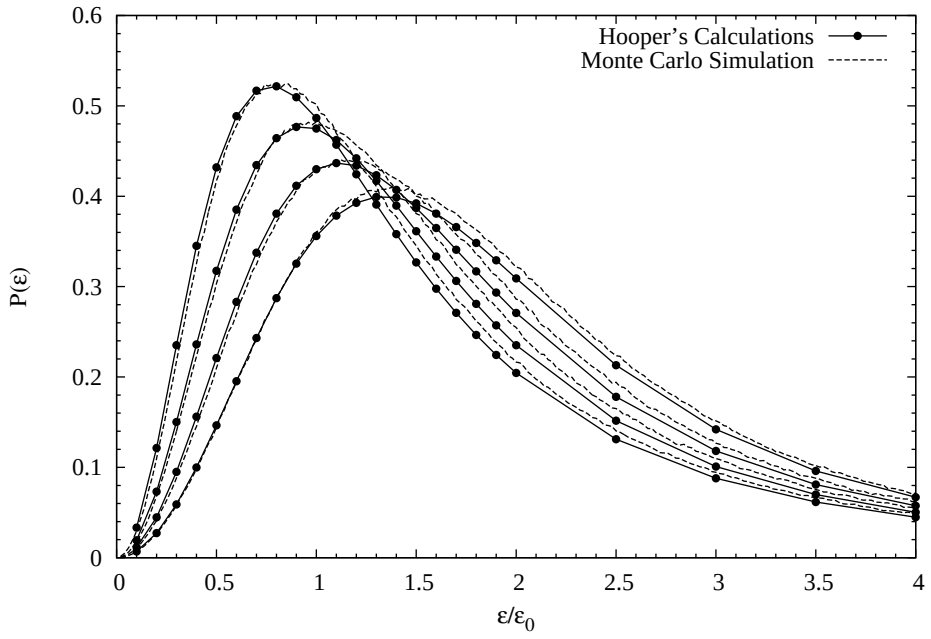

Figure 6.10: Monte Carlo simulation of the static electric field, $a = l_{typ}/r_{Debye}$. Dark lines with points are Hooper's calculation, while my calculation is the dashed line. This comparison shows that my simulation tends to favor larger electric fields more than Hooper's distribution. Disagreement is at most 4%.

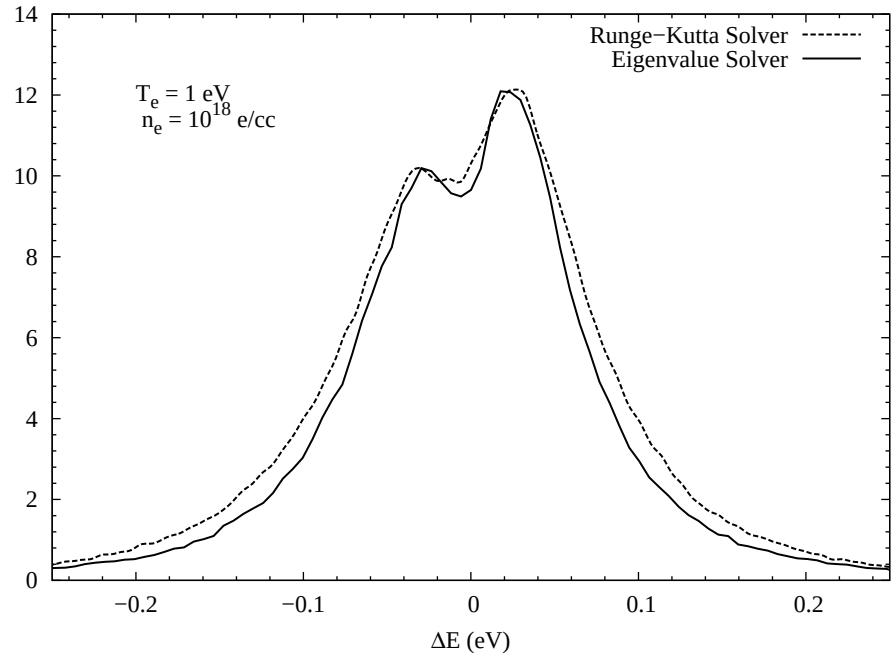

Figure 6.11: Hβ at high density, where field ionization and quenching collisions will be important. Both profiles show the blue side of the core enhanced and the blue wing diminished compared to the red side of the profile. The Runge-Kutta integrator shows a slightly wider profile, yet nearly identical shape. The RK method does not guarantee unitarity and can introduce broadening that is numerical in nature [10].

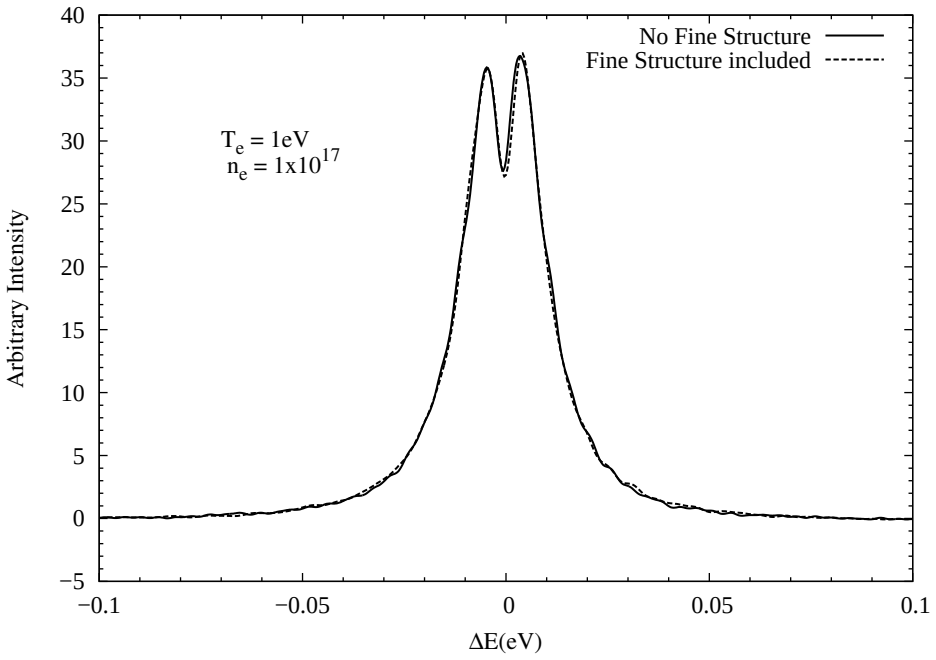

Figure 6.12: Comparison of $H\beta$ with and without fine structure included for two different densities.

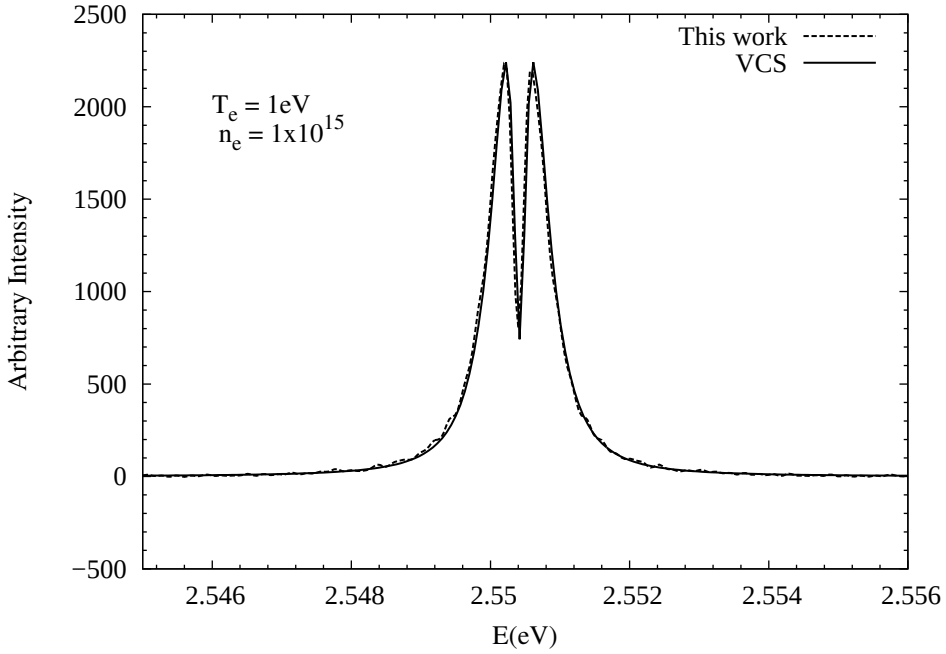

Figure 6.13: Low density ($n_e = 10^{15}$) comparison of this work with VCS. The agreement is quite good (except for numerical noise).

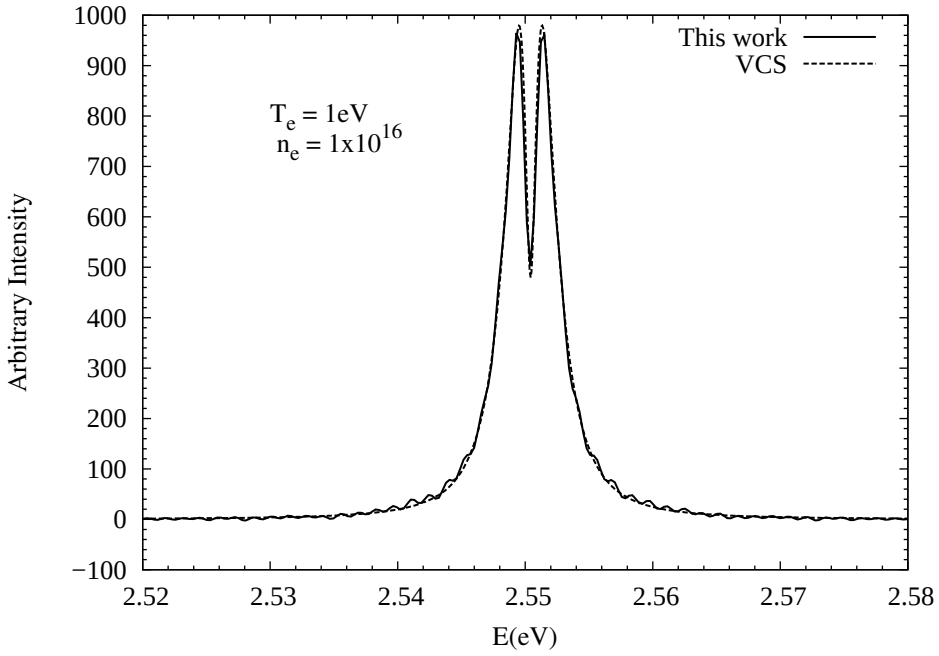

Figure 6.14: $n_e = 10^{16}$ comparison of this work with VCS. The work presented here is for the same set of approximations used by VCS.

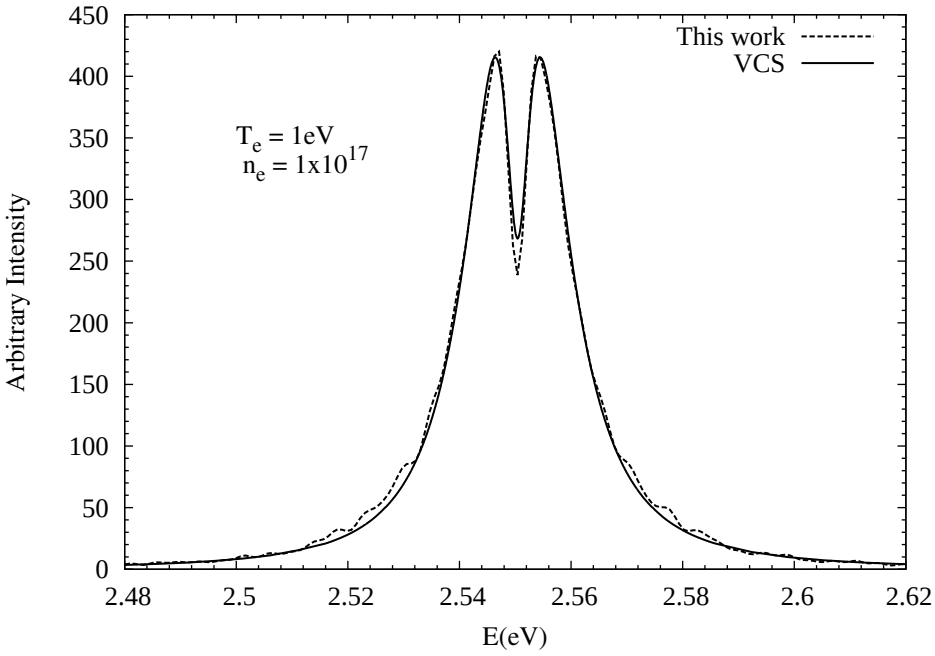

Figure 6.15: My calculated Hβ line profile compared to VCS. The shapes and widths are nearly identical, like in figure 6.13. The calculation agrees with Hβ over 3 orders of magnitude. This is essential with Hβ being the standard line where most theories agree.

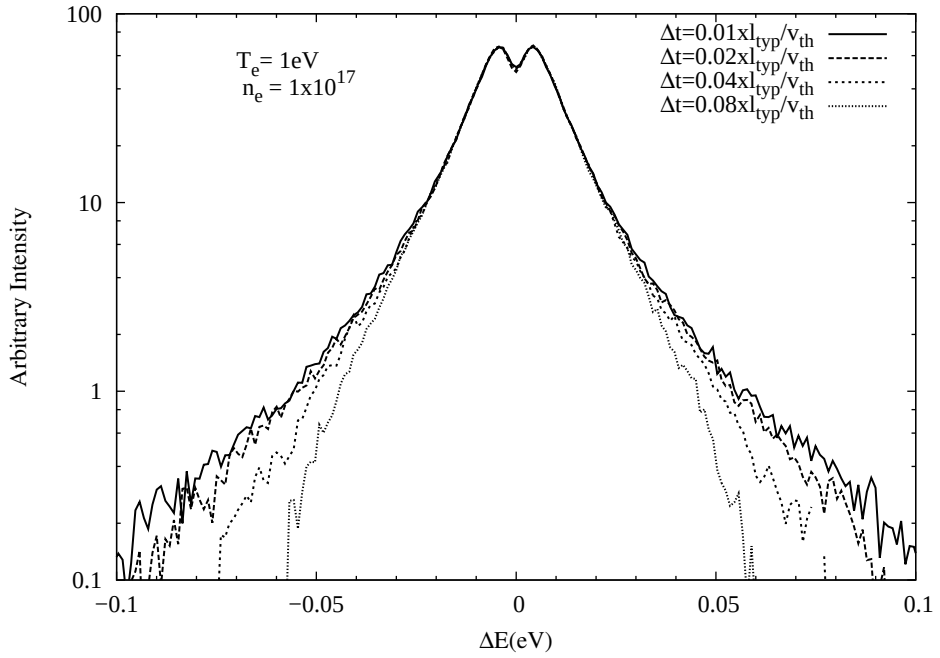

Figure 6.16: When I vary the time-step in the calculation, the wings become diminished somewhat. When I calculate profiles for WD atmospheres, I need to use small $\Delta\ t$ in order to properly calculate the wings of the line.

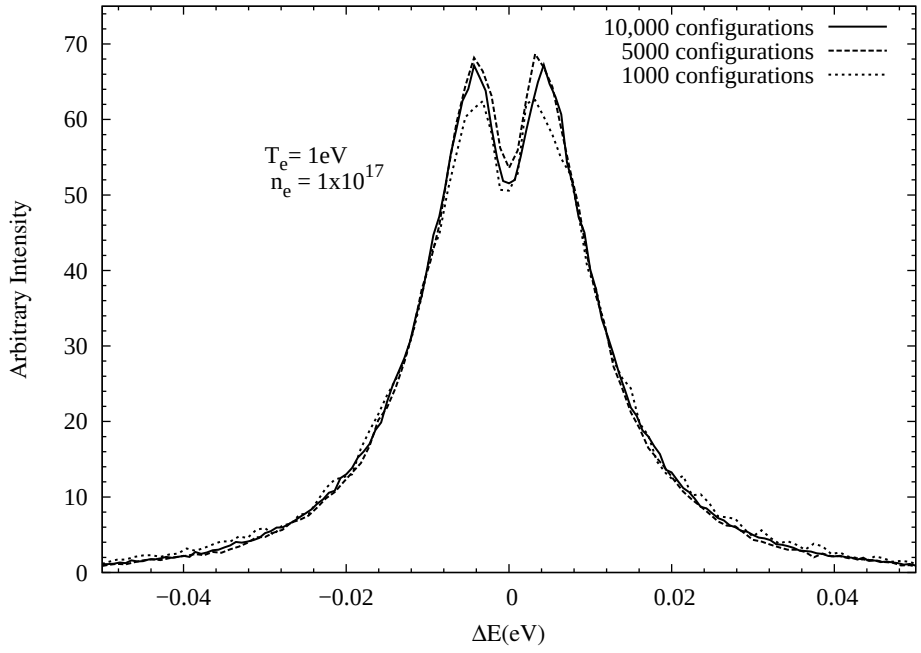

Figure 6.17: Hβ with different number of configurations. Obviously, the fewer configurations averaged the noisier the profile becomes. However, the FWHM is well defined even for few iterations. Even at low number of configurations, the profile's FWHM is well defined. But it will take many configurations to fully resolve the central structure of the profile.

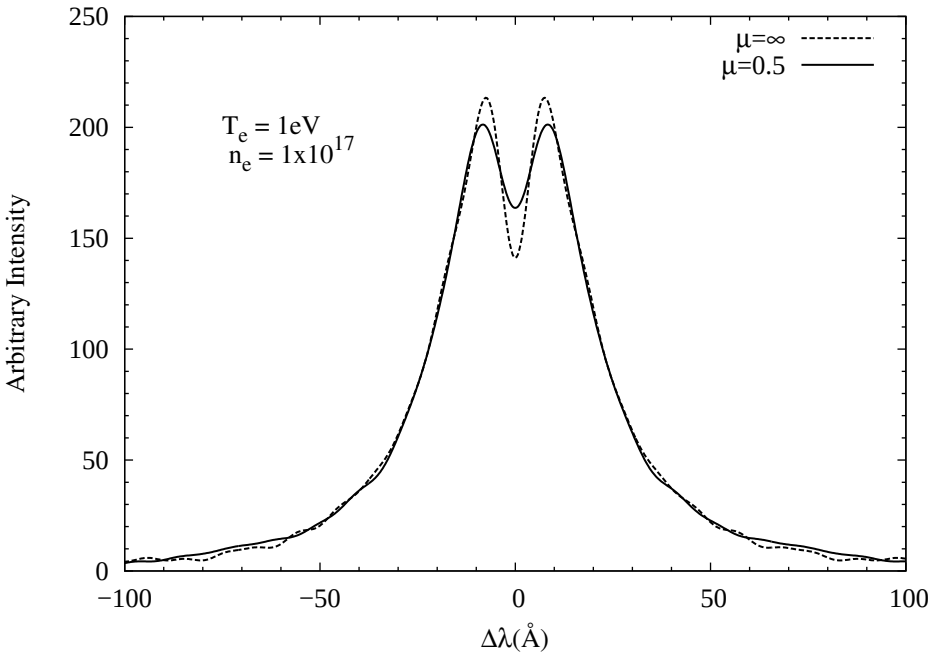

Figure 6.18: I compare two models of the ions. Dark line: dynamic ions according to the "μ-ion model". Dotted line: static ions. The effects of ion motions are apparent, the features of the profile are filled in or blurred. In this example, I show how ion dynamics blur the Hβ line where the central dip is not as prominent.

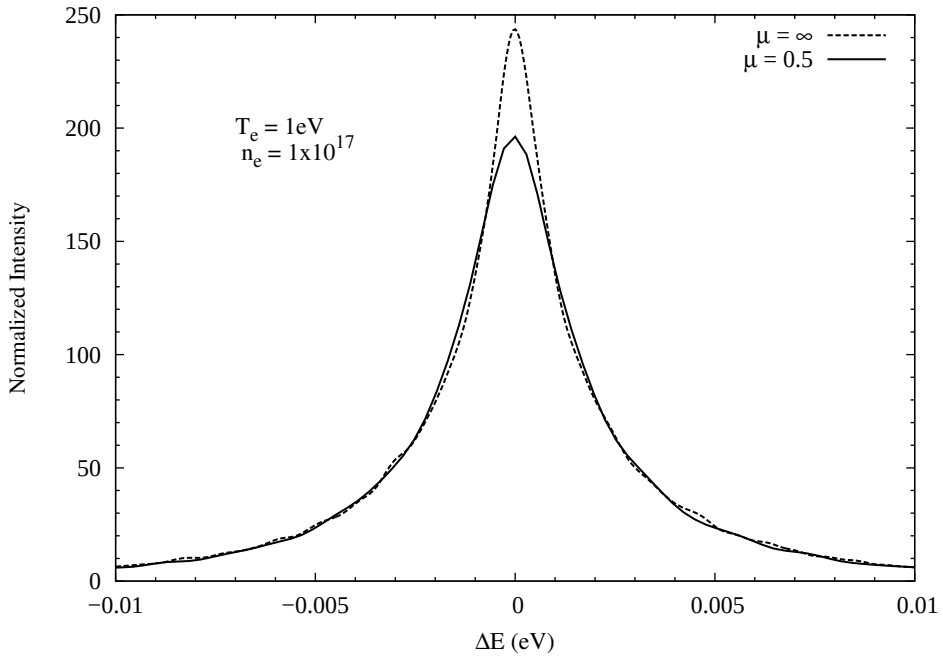

Figure 6.19: The effect of dynamic ions ($\mu = 0.5$) is much more significant for Hα. The FWHM of the profile that includes dynamic ions is 66% greater than the static ion case.

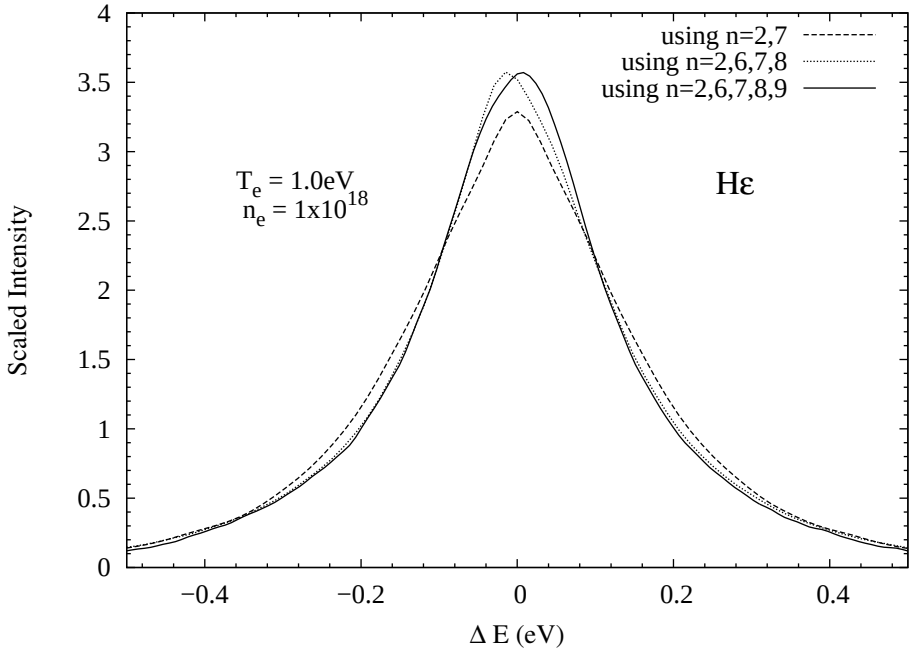

Figure 6.20: Demonstrating the effects of including different n states in the calculation. The profiles are area normalized. The full-width at half maximum decreases by 17% when including the nearby states.

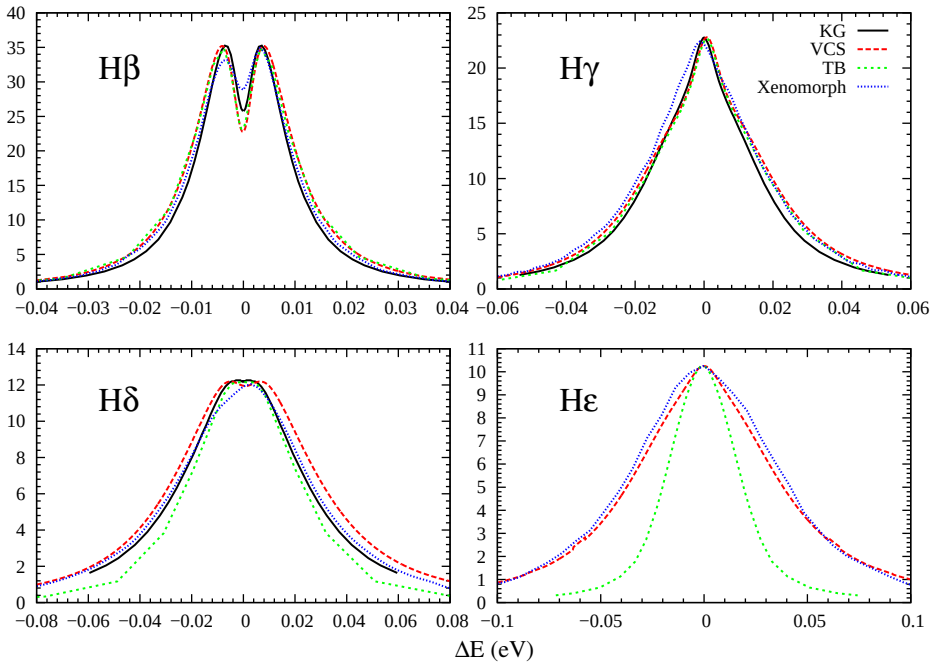

Figure 6.21: Comparing Xenomorph (including ion dynamics and quenching collisions) with KG, VCS, and TB09 for Hβ through Hϵ. At $n_e = 10^{17}$, there are minor differences between the different theories for Hβ and Hϵ. Xenomorph is the only one to not predict a central dip for Hδ. Xenomorph does predict substantial asymmetries, and significant reduction in FWHM for Hδ and Hϵ.

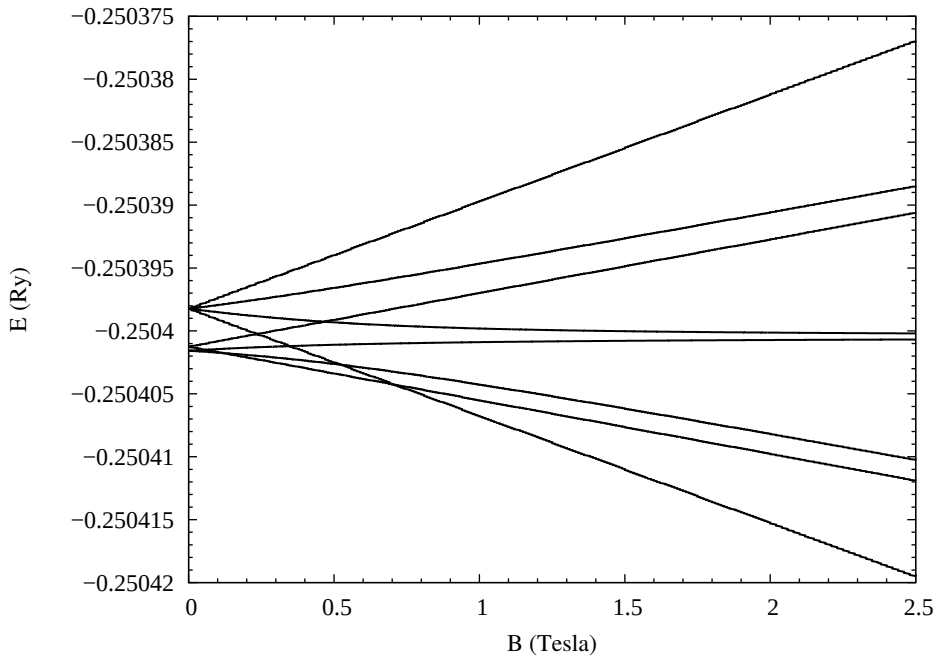

Figure 6.22: The splitting of the $n = 2$ level of H, including fine structure and Lamb shift. Notice how the diverging lines do not avoid each other as they do in the Stark effect. At high fields, the lines do change to align with some other level splitting (Paschen-Back effect)

.

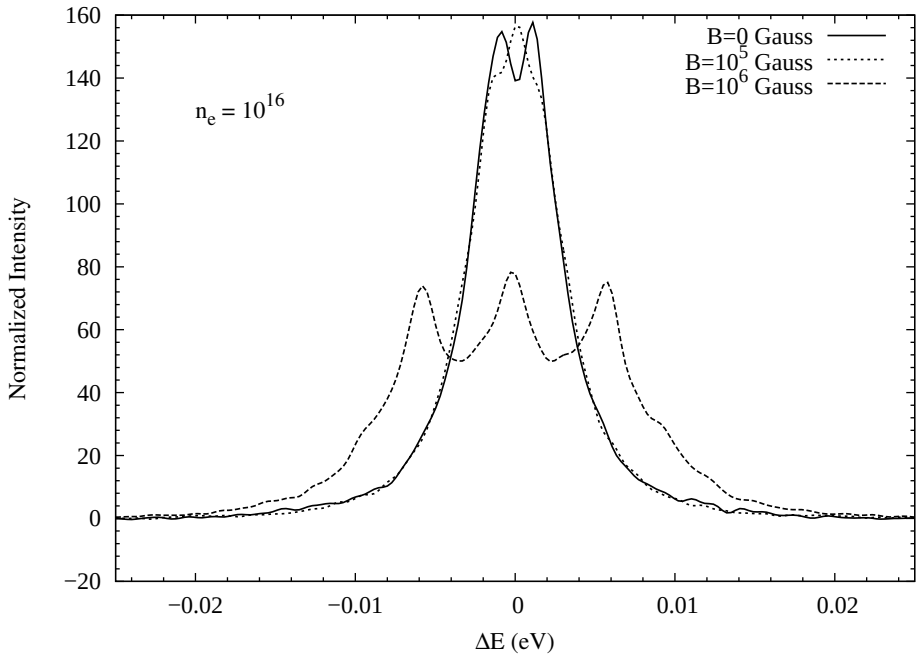

Figure 6.23: Hβ for several different B field values. The magnetic field is not detectable for electric fields below about 10^5 Gauss.

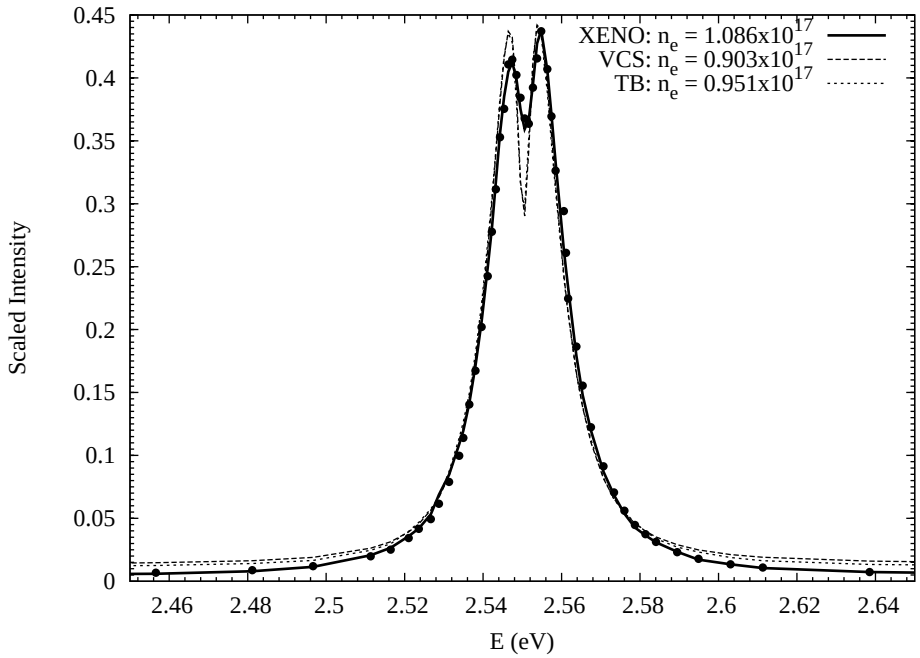

Figure 6.24: Hβ profile fits against Wiese et al. (1972), an experiment used for benchmarking profiles. The observed features are reproduced, such as the enhancement of the red wing, the blue enhancement of the blue core and the filling in of the central dip. Because VCS and TB09 have not included these effects, they over predict the central dip. Neither VCS or TB09 can account for the asymmetry

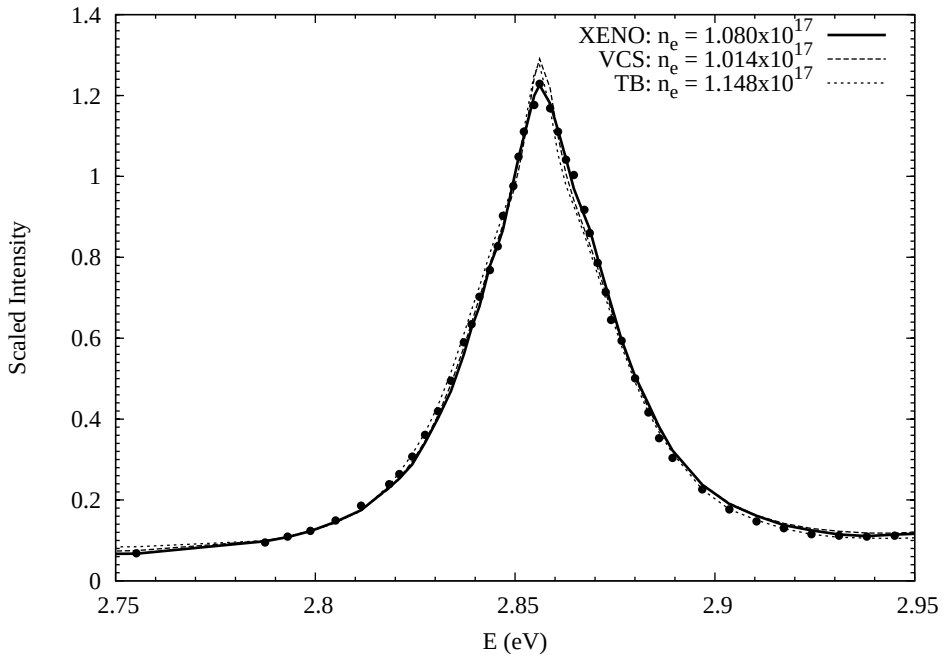

Figure 6.25: Hγ profiles are fitted Wiese et al. (1972). The different theories tend to agree well on the shape since the effects of ion motion are less relevant. However, the derived densities between the Hβ and Hγ are different for VCS and TB09

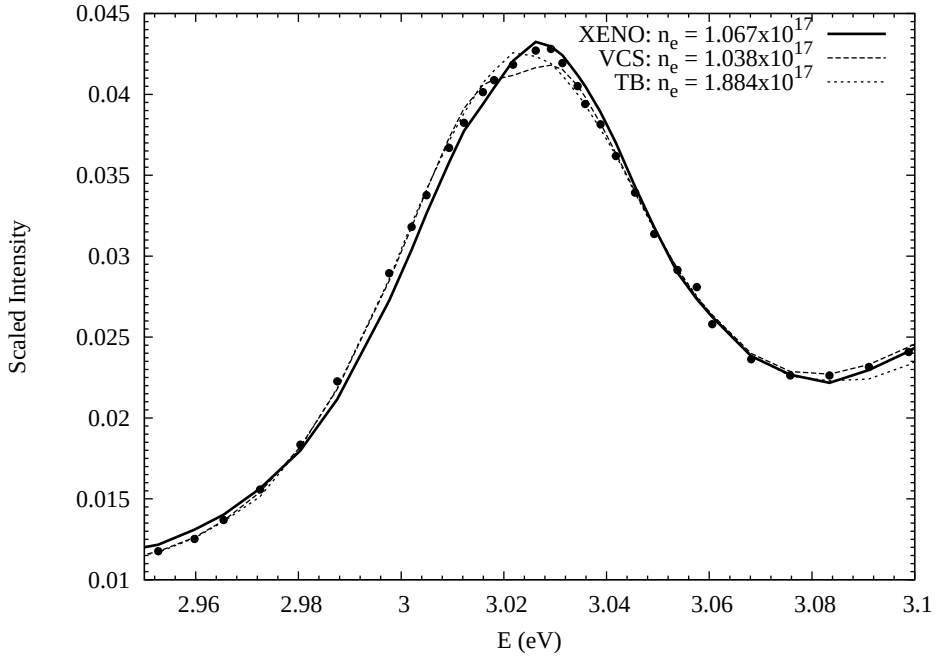

Figure 6.26: Hδ profiles fitted against Wiese et al. (1972). Here, TB09 and VCS do a little better in the wings, but the core structure is missed completely. Xenomorph reproduces the core structure and most importantly is the only theory where the derived density is consistent between the three lines used.

Appendices

Appendix A

Bra-Ket Notation

In general, quantum mechanical states are described by a large basis set and there are many possible wave-functions that an electron can take. As a result, matrix formalism has been employed by Heisenberg and Dirac to describe quantum systems. A state would be described as a vector with some probability that the electron is in one of those states. Those states could be a pure state (be described by one wavefunction) or can be described by a linear combination of wavefunctions. Dirac used the notation $|\vdots\rangle$ (Bra) to describe a state vector and $\langle\vdots|$ (Ket) is it's complex conjugate:

$$|\psi\rangle = \begin{pmatrix} \psi_1 \\ \psi_2 \\ \psi_3 \\ \vdots \end{pmatrix} \quad \& \quad \langle\psi| = \begin{pmatrix} \psi_1^* & \psi_2^* & \psi_3^* & \dots \end{pmatrix}. \tag{A.1}$$

Each ψ_i forms an orthogonal basis set. $\langle\psi_i|\psi_j\rangle$ is a dot product which involves an integral over the spatial coordinates. Since the states are orthogonal, $\langle\psi_i|\psi_j\rangle = \delta_{ij}$.

In quantum mechanics, observables are the result of operators on eigenstates, for example, the Hamiltonian is an energy operator, whose observable is the energy of the system. Operators can then be described by matrices and

satisfy the eigenvalue problem:

$$A|\psi\rangle = a|\psi\rangle. \tag{A.2}$$

Any matrix element of an operator will be denoted $\langle\psi|A|\psi\rangle$.

Appendix B

Quantum Pictures

B.1 Schrödinger Picture

In the Schrödinger picture of quantum evolution, the eigenvectors evolved in time, leaving the operators (usually) not a function of time. Therefore the Schrödinger equation ($\hbar = 1$)

$$i\frac{d}{dt}\psi = H\psi \tag{B.1}$$

has the solution where $|\psi(t)\rangle = e^{-iHt}|\psi(0)\rangle$. A time evolution operator may be defined so that

$$|\psi(t)\rangle = U(t)|\psi(0)\rangle \tag{B.2}$$

B.2 Heisenberg Picture

Heisenberg, on the other hand had a picture where the operators evolved in time and the eigenvectors remained independent of time. This is a convenient picture to work in for matrix mechanics. In either picture you can define the time evolution of some observable

$$a(t) = \langle\psi(0)|e^{iHt}Ae^{-iHt}|\psi(0)\rangle \tag{B.3}$$

where $e^{-iHt}|\psi(0)\rangle$ is the time evolution in the Schrödinger picture. Heisenberg then went on to define

$$A(t) = e^{iHt}A(0)e^{-iHt} \tag{B.4}$$

so that the operators evolve rather than the eigenstates.

B.3 Interaction Picture

The interaction picture takes the best of both worlds by evolving both the operators and the eigenvectors, but taking some of the trivial oscillations out of the solution:

$$|\psi_I(t)\rangle = e^{iHt}|\psi_S\rangle^1 \tag{B.5}$$

where the subscripts I and S denote the interaction and Schrödinger pictures, respectively. This makes simplifies the Schrödinger equation when solving for a system that has a known Hamiltonian, H_0 and a time dependent part, $V(t)$.

The Schrödinger equation for such a system is

$$i\frac{d}{dt}|\psi_S\rangle = [H_0 + V(t)]|\psi_S\rangle. \tag{B.6}$$

Taking Eq (B.5) into Eq (B.6) yeilds

$$i\frac{d}{dt}|e^{-iH_0t}\psi_I\rangle = [H_0 + V(t)]e^{-iH_0t}|\psi_I\rangle, \tag{B.7}$$

which can be manipulated so that

$$H_0e^{-iH_0t}|\psi_I\rangle + ie^{-iH_0t}\frac{d}{dt}|\psi_I\rangle = [H_0e^{-iH_0t} + V(t)e^{-iH_0t}]|\psi_I\rangle. \tag{B.8}$$

[1]Notice the sign of this equation compared to the Schrödinger picture

Manipulating the exponentials and the unperturbed Hamiltonians brings something similar to the Heisenberg representation,

$$i\frac{d}{dt}|\psi_I\rangle = [e^{iH_0t}H_0e^{-iH_0t} + e^{iH_0t}V(t)e^{-iH_0t} - H_0]|\psi_I\rangle. \tag{B.9}$$

Becuase $e^{iH_0t}H_0e^{-iH_0t} = H_0$ then the Schrödinger equation for the interaction picture is written

$$i\frac{d}{dt}|\psi_I\rangle = V_I(t)|\psi_I\rangle, \tag{B.10}$$

where $V_I(t) = e^{iH_0t}V_S(t)e^{-iH_0t}$.

Appendix C

Racah Algebra

C.1 Irreducible Tensor Operators

I have been using the Racah formalism introduced in Cowan's book on Atomic Physics and Spectroscopy. Tensors can be decomposed to what are "irreducible parts", which can transform under a rotation of coordinates. This is analogous to changing from Cartesian coordinates to spherical harmonics. The tensors will be an operator $T^{(k)}$ that has 2k+1 components with q going from -k to k. Individual components of the tensor will be denoted $T_q^{(k)}$. And the operator is Hermitian if $T_q^{(k)\dagger} = (-1)^q T_q^{(k)}$

This project will largely be concerned with dipole operators, which can be re-written in terms of irreducible tensor operators. Table C.1 has the tensor of rank 1, with q values $\pm 1, 0$. This is analogous to 3D cartesian coordinate system (column 2) or a spherical coordinate system (column 3).

Table C.1: Tensor Operator transformations

$T_{-1}^{(1)}$	$\frac{1}{\sqrt{2}}(D_x - \mathrm{i}D_y)$	$\frac{1}{\sqrt{2}} D \sin\theta e^{\mathrm{i}\phi}$
$T_0^{(1)}$	D_z	$D\cos\theta$
$T_1^{(1)}$	$-\frac{1}{\sqrt{2}}(D_x + \mathrm{i}D_y)$	$\frac{1}{\sqrt{2}} D \sin\theta e^{-\mathrm{i}\phi}$

C.2 Wigner-Eckart Theorem

The Wigner-Eckart theorem takes the formalism of irreducible tensor operators and re-writes the components of the operator as

$$\langle \alpha J M | T_q^{(k)} | \alpha' J' M' \rangle = (2J+1)^{-1/2} C_{jm}^{j' k m' q} \langle \alpha J \| T^{(k)} \| \alpha' J' \rangle \tag{C.1}$$

Where $\langle \alpha J || T^{(k)} || \alpha' J' \rangle$ is the reduced operator that depends only on the radial part of the function. The Clepsh-Gordon Coefficient, $C_{jm}^{j' k m' q}$ is the angular part of the calculation that transforms the operator into the individual components (Table C.1).

$$C_{j_3 m_3}^{j_1 k m_1 q} = (2j_3+1)(-1)^{j_1 - j_2 + m_3} \begin{pmatrix} j_1 & k & j_3 \\ m_1 & q & m_3 \end{pmatrix}$$

C.2.1 3j Symbols

The Clepsh-Gordon Coefficient is a 3j symbol that can be written as

$$\begin{pmatrix} j_1 & j_2 & j_3 \\ m_1 & m_2 & m_3 \end{pmatrix} = \delta_{m_1+m_2+m_3,0} (-1)^{j_1 - j_2 - m_3} \times$$
$$\Big\{ (j_1+j_2-j_3)!(-j_1+j_2+j_3)!(j_1-m_1)!(j_1+m_1)!$$
$$(j_2-m_2)!(j_2+m_2)!(j_3-m_3)!(j_3+m_3)![(j_1+j_2+j_3+1)!]^{-1} \Big\}^{1/2} \tag{C.2}$$
$$\times$$
$$\sum_k (-1)^k \Big\{ k!(j_1+j_2-j_3-k)!(j_1-m_1-k)!$$
$$(j_2+m_2-k)!(j_3-j_2+m_1+k)!(j_3-j_1-m_2+k)! \Big\}^{-1}$$

Where $max(0, j_2 - j_3 - m_1, j_1 - j_3 + m_2) \leq k \leq min(j_1 + j_2 - j_3, j_1 - m_1, j_2 + m_2)$

Here are some interesting selection rules. The sum of the m_i in the 3j symbol have to equal zero, or the 3j symbol is zero. For dipole moments, $m_1 = -M$ and $m_3 = M'$, and m_2 is set to -1, 0, or 1, this corresponds to dipole transitions of $-\sigma, \pi, +\sigma$ transitions where $M' = M$ for π transitions.

C.2.2 6j Symbols

The 6j symbol is a five-fold summation over a product of four 3j symbols and can be written in the form:

$$\left\{ \begin{array}{ccc} j_1 & j_2 & j_3 \\ l_1 & l_2 & l_3 \end{array} \right\} = \Delta(j_1, j_2, j_3)\Delta(j_1, l_2, l_3)\Delta(l_1, j_2, l_3)\Delta(l_1, l_2, j_3)\times$$
$$\sum_k \left[\frac{(-1)^k (k+1)!}{(k - j_1 - j_2 - j_3)!(k - j_1 - l_2 - l_3)!(k - l_1 - j_2 - l_3)!(k - l_1 - l_2 - j_3)!} \right.$$
$$\left. \times \frac{1}{(j_1 + j_2 + l_1 + l_2 - k)!(j_2 + j_3 + l_2 + l_3 - k)!(j_3 + j_1 + l_3 + l_1 - k)!} \right] \tag{C.3}$$

The Δ functions are defined as

$$\Delta(j_1, j_2, j_3) = \sqrt{\frac{(j_1 + j_2 - j_3)!(j_1 - j_2 + j_3)!(-j_1 + j_2 + j_3)!}{(j_1 + j_2 + j_3 + 1)!}} \tag{C.4}$$

The sum in equation (C.3) is over k, where k is between $max(j_1 + j_2 + j_3, j_1 + l_2 + l_3, l_1 + j_2 + l_3, l_1 + l_2 + j_3) \leq k \leq min(j_1 + j_2 + l_1 + l_2, j_2 + j_3 + l_2 + l_3, j_3 + j_1 + l_3 + l_1)$. As with the 3j symbols, each factorial argument must be greater than zero or the 6j symbol is zero. The 6j symbol is used more for coupling two angular momenta together, for example, it can be used for LS

coupling, which is important for fine structure and caclulating Zeeman matrix elements.

Appendix D

Magnetic Fields

Another effect important to WD photospheres is a magnetic field, so this section briefly looks at the effect of magnetic fields on line shapes. The broadening due to the Stark effect will dominate the line shape until the splitting of the Zeeman effect becomes greater than the average splitting due to nearby electric fields. This would mean that magnetic fields could be present but not detectable without high resolution spectroscopy. The matrix elements of the magnetic Hamiltonian are diagonal in M,L,S, but not J (Cowan's Notation):

$$\begin{aligned}\langle \alpha LSJM|H_{mag}|\alpha' L'S'J'M'\rangle = B\mu_0 \big[M\delta_{\alpha LSJM,\alpha' L'S'J'M'} \quad - \\ (g_s-1)(-1)^{L+S+M}\sqrt{(2J+1)(2J'+1)S(S+1)(2S+1)} \\ \times\delta_{\alpha LSM,\alpha' L'S'M'} \begin{pmatrix} J & 1 & J' \\ -M & 0 & M' \end{pmatrix} \begin{Bmatrix} L & S & J \\ 1 & J' & S \end{Bmatrix} \big].\end{aligned} \tag{D.1}$$

All these terms with S, J, M in both the diagonal and off-diagonal elements are from the evaluation of 3j and 6j symbols. The anomalous gyromagnetic ratio is $g_s \cong 2.0023$. The constant is evaluated at $\mu_0 = \frac{e\hbar}{2mc} = 4.2543 \times 10^{-10} Ry/Gauss$. The splitting of the $n = 2$ level is shown in Figure

6.22. In the weak field limit, the Zeeman effect is a small splitting in the energy levels and all quantum numbers are still good numbers to describe a state. However, in the strong limit, both S and L process around B (chosen to be aligned with the z-axis, making J no longer a good quantum number. Because I am numerically evaluating the Hamiltonian, I need not take limits of the eigenvalues as is done in perturbation theory approximations.

The nearly diagnonal nature of the Zeeman effect does not give rise to configuration mixing in the same way that the Stark effect does (See Figure 6.2). Due to the transition selection rules of the 3j symbol in radiative transitions, the degeneracy between π and σ transitions will be broken. At high values of magnetic fields, which we will encounter in WDs, the transitions will form a triplet, known as the Paschen-Back effect. The π (z-polarized) transition will be the central component and the σ (xy-circularly polarized) transitions will be to the blue and red sides of the π transition. This may be interesting in observing polarizations in WDs.

This is interesting because magnetic fields break the degeneracy in M, therefore the behavior seen in Figure 6.1 due to fine structure is amplified with the increase in degeneracy. Unlike before, with the pure Stark effect, there will not be a degeneracy between positive and negative m values. This will change the evolution of the states. Therefore, the behavior of the energy levels with increasing electric field will be non-linear with a non-zero magnetic field.

Figure 6.23 Shows the evolution of Hβ with increasing B field from 0 Gauss to 10^6 Gauss. Notice that at $n_e = 1 \times 10^{16}$ there is enough Stark broad-

ening to not notice a significant change in the line shape until the magnetic field is 10^5 Gauss.

Calculating Stark and Zeeman profiles simultaneously requires a numerical solution, which may explain why not many have done this calculation or have approximated this calculation. This also leads to a prediction that for the current set-up at Sandia National Laboratories (or any laboratory) that it will be incredibly difficult to observe magnetic fields in our current set-up. The Zeeman splitting must be of the same order of magnitude as the mean E field induced by the nearby perturbers.

Bibliography

[1] S. Alexiou and A. Poquérusse. Standard line broadening impact theory for hydrogen including penetrating collisions. *Phys. Rev. E*, 72(4):046404, October 2005.

[2] P. W. Anderson. Pressure Broadening in the Microwave and Infra-Red Regions. *Physical Review*, 76:647–661, September 1949.

[3] M. Baranger. General Impact Theory of Pressure Broadening. *Physical Review*, 112:855–865, November 1958.

[4] M. Baranger. Problem of Overlapping Lines in the Theory of Pressure Broadening. *Physical Review*, 111:494–504, July 1958.

[5] M. Baranger. Simplified Quantum-Mechanical Theory of Pressure Broadening. *Physical Review*, 111:481–493, July 1958.

[6] M. Baranger and B. Mozer. Electric Field Distributions in an Ionized Gas. *Physical Review*, 115:521–525, August 1959.

[7] M. Baranger and B. Mozer. Electric Field Distributions in an Ionized Gas. II. *Physical Review*, 118:626–631, May 1960.

[8] H. A. Bethe and E. E. Salpeter. *Quantum Mechanics of One- and Two-Electron Atoms*. 1957.

[9] R. D. Cowan. *The theory of atomic structure and spectra*. 1981.

[10] S. Djurović, M. Ćirišan, A. V. Demura, G. V. Demchenko, D. Nikolić, M. A. Gigosos, and M. Á. González. Measurements of H Stark central asymmetry and its analysis through standard theory and computer simulations. *Phys. Rev. E*, 79(4):046402, April 2009.

[11] A. Einstein. Zur Quantentheorie der Strahlung. *Physikalische Gesellschaft Zürich*, 18:47–62, 1916.

[12] R. E. Falcon, D. E. Winget, M. H. Montgomery, and K. A. Williams. A Gravitational Redshift Determination of the Mean Mass of White Dwarfs. DA Stars. *ApJ*, 712:585–595, March 2010.

[13] M. A. Gigosos and V. Cardeñoso. New plasma diagnosis tables of hydrogen Stark broadening including ion dynamics. *Journal of Physics B Atomic Molecular Physics*, 29:4795–4838, October 1996.

[14] M. A. Gigosos and V. Cardenoso. Study of the effects of ion dynamics on Stark profiles of Balmer-α and -β lines using simulation techniques. *Journal of Physics B Atomic Molecular Physics*, 20:6005–6019, November 1987.

[15] M. A. Gigosos, V. Cardenoso, and F. Torres. Stark-broadening simulation in hydrogen - Study of the binary and complete binary collision hypotheses. *Journal of Physics B Atomic Molecular Physics*, 19:3027–3033, October 1986.

[16] M. A. Gigosos, J. Fraile, and F. Torres. Hydrogen Stark profiles: A simulation-oriented mathematical simplification. *Phys. Rev. A*, 31:3509–3511, May 1985.

[17] M. A. Gigosos and M. Á. González. Calculations of the polarization spectrum by two-photon absorption in the hydrogen Lyman-α line. *Phys. Rev. E*, 58:4950–4959, October 1998.

[18] M. A. Gigosos, M. Á. González, and N. Konjević. On the Stark broadening of Sr^+ and Ba^+ resonance lines in ultracold neutral plasmas. *European Physical Journal D*, 40:57–63, October 2006.

[19] H. R. Griem. Principles of plasma spectroscopy. *Proceedings of the Physical Society*, 1997.

[20] H. R. Griem, A. C. Kolb, and K. Y. Shen. Stark Broadening of Hydrogen Lines in a Plasma. *Physical Review*, 116:4–16, October 1959.

[21] C. F. Hooper. Low-Frequency Component Electric Microfield Distributions in Plasmas. *Physical Review*, 165:215–222, January 1968.

[22] D. G. Hummer and D. Mihalas. The equation of state for stellar envelopes. I - an occupation probability formalism for the truncation of internal partition functions. *ApJ*, 331:794–814, August 1988.

[23] S. O. Kepler, S. J. Kleinman, A. Nitta, D. Koester, B. G. Castanheira, O. Giovannini, A. F. M. Costa, and L. Althaus. White dwarf mass distribution in the SDSS. *MNRAS*, 375:1315–1324, March 2007.

[24] P. Kepple and H. R. Griem. Improved Stark Profile Calculations for the Hydrogen Lines Hα, Hβ, Hγ, and Hδ. *Physical Review*, 173:317–325, September 1968.

[25] D. P. Kilcrease, R. C. Mancini, and C. F. Hooper, Jr. Ion broadening of dense-plasma spectral lines including field-dependent atomic physics and the ion quadrupole interaction. *Phys. Rev. E*, 48:3901–3913, November 1993.

[26] A. E. Kramida. A critical compilation of experimental data on spectral lines and energy levels of hydrogen, deuterium, and tritium. *Atomic Data and Nuclear Data Tables*, 96:586–644, November 2010.

[27] M. Lemke. Extended VCS Stark broadening tables for hydrogen – Lyman to Brackett series. *A&AS*, 122:285–292, April 1997.

[28] R. C. Mancini, D. P. Kilcrease, L. A. Woltz, and C. F. Hooper. Calculational aspects of the Stark line broadening of multielectron ions in plasmas. *Computer Physics Communications*, 63:314–322, February 1991.

[29] W. Olchawa, R. Olchawa, and B. Grabowski. Stark broadening of hydrogen spectral lines with fine structure effects. *European Physical Journal D*, 28:119–124, January 2004.

[30] W. H. Press, S. A. Teukolsky, W. T. Vetterling, and B. P. Flannery. *Numerical recipes in C++ : the art of scientific computing*. 2002.

[31] M. J. Seaton. Atomic data for opacity calculations. XIII - Line profiles for transitions in hydrogenic ions. *Journal of Physics B Atomic Molecular Physics*, 23:3255–3296, October 1990.

[32] E. W. Smith, J. Cooper, and C. R. Vidal. Unified Classical-Path Treatment of Stark Broadening in Plasmas. *Physical Review*, 185:140–151, September 1969.

[33] E. Stambulchik, D. V. Fisher, Y. Maron, H. R. Griem, and S. Alexiou. Correlation effects and their influence on line broadening in plasmas: Application to H. *High Energy Density Physics*, 3:272–277, May 2007.

[34] E. Stambulchik and Y. Maron. A study of ion-dynamics and correlation effects for spectral line broadening in plasma: K-shell lines. *J. Quant. Spec. Radiat. Transf.*, 99:730–749, May 2006.

[35] R. Stamm, Y. Botzanowski, V. P. Kaftandjian, B. Talin, and E. W. Smith. Ion dynamics effect on hydrogenic Stark profiles in hot and dense plasmas. *Physical Review Letters*, 52:2217–2220, June 1984.

[36] R. Stamm and E. W. Smith. Computer simulation technique for plasmas. *Phys. Rev. A*, 30:450–453, July 1984.

[37] R. Stamm, E. W. Smith, and B. Talin. Study of hydrogen Stark profiles by means of computer simulation. *Phys. Rev. A*, 30:2039–2046, October 1984.

[38] R. Stamm and B. Talin. Microfield simulation applied to the calculation of Stark profiles. *Annales de Physique*, 9:687–695, 1984.

[39] P.-E. Tremblay and P. Bergeron. Spectroscopic Analysis of DA White Dwarfs: Stark Broadening of Hydrogen Lines Including Nonideal Effects. *ApJ*, 696:1755–1770, May 2009.

[40] C. R. Vidal, J. Cooper, and E. W. Smith. Hydrogen Stark broadening calculations with the unified classical path theory. *J. Quant. Spec. Radiat. Transf.*, 10:1011–1063, 1970.

[41] C. R. Vidal, J. Cooper, and E. W. Smith. Unified theory calculations of Stark broadened hydrogen lines including lower state interactions. *J. Quant. Spec. Radiat. Transf.*, 11:263–281, 1971.

[42] C. R. Vidal, J. Cooper, and E. W. Smith. Hydrogen Stark-Broadening Tables. *ApJS*, 25:37, January 1973.

[43] W. L. Wiese, D. E. Kelleher, and V. Helbig. Variations in Balmer-line Stark profiles with atom-ion reduced mass. *Phys. Rev. A*, 11:1854–1864, June 1975.

[44] W. L. Wiese, D. E. Kelleher, and D. R. Paquette. Detailed Study of the Stark Broadening of Balmer Lines in a High-Density Plasma. *Phys. Rev. A*, 6:1132–1153, September 1972.